Augmented reality assisted orthopaedic surgery

by

Gareth Holmes

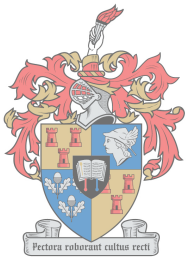

Thesis presented in partial fulfilment of the requirements for the degree of Master of Engineering (Mechanical) in the Faculty of Engineering at Stellenbosch University

Supervisor: Mr. J. van der Merwe
Co-supervisor: Dr. DJ. van den Heever

March 2018

Declaration

By submitting this thesis electronically, I declare that the entirety of the work contained therein is my own, original work, that I am the sole author thereof (save to the extent explicitly otherwise stated), that reproduction and publication thereof by Stellenbosch University will not infringe any third party rights and that I have not previously in its entirety or in part submitted it for obtaining any qualification.

Date: ..... March 2018 .....

Abstract

Augmented reality assisted orthopaedic surgery

G. Holmes

Department of Mechanical and Mechatronic Engineering,
University of Stellenbosch,
Private Bag X1, Matieland 7602, South Africa.

Thesis: MEng (Mech)

March 2018

The aim of this study was to investigate the clinical efficacy and feasibility of an application of augmented reality assisted orthopaedic surgery (ARAOS) technology that focuses on supporting and enhancing current best practices in orthopaedic surgery. Through consultation with a representative from the Advanced Orthopaedic Training Centre at Tygerberg Hospital, wrist replacement surgery was chosen as the clinical problem on which to focus. A workflow aimed at providing maximum benefit for these types of procedures was conceptualised which involved making use of the two surgically removed bones to predict the remaining geometry by incorporating a statistical shape model into a shape estimation process. A simulated procedure based around one aspect of wrist replacement surgery was designed which allowed for a comparison to be made between using conventional navigational methods and that of using AR guidance to assist with surgical navigation. The results from this experiment indicate marginally inferior accuracy compared to the more conventional fluoroscopic guidance. However, a reduction in procedural time, and a relatively short learning curve (intuitiveness) was observed when using AR guidance. Furthermore, with AR navigational assistance, both the patient and the surgeon are not exposed to harmful ionising radiation sources. In conclusion, it is the author's opinion that ARAOS technology appears to show clinical efficacy and feasibility for use in the operating room with potential to support and enhance current best practises in orthopaedic surgery while remaining affordable and potentially more intuitive than other forms of navigational assistance.

Uittreksel

Aangevulderealiteit-gesteunde ortopediese chirurgie-tegnologie

("Augmented reality assisted orthopaedic surgery")

G. Holmes

Departement Meganiese en Megatroniese Ingenieurswese,
Universiteit van Stellenbosch,
Privaatsak X1, Matieland 7602, Suid Afrika.

Tesis: MIng (Meg)

Maart 2018

Die oogmerk met hierdie studie was 'n ondersoek na die kliniese doeltreffendheid en uitvoerbaarheid van 'n toepassing van aangevulderealiteit-gesteunde ortopediese chirurgie-tegnologie (augmented reality assisted orthopaedic surgery [ARAOS] in Engels) wat bedoel is om bestaande beste praktyk in ortopediese chirurgie te ondersteun en te verbeter. Ná oorlegpleging met 'n verteenwoordiger van die Gevorderde Ortopediese Opleidingsentrum by die Tygerberghospitaal is polsgewrigvervangingschirurgie gekies as die kliniese probleem waarop daar in hierdie bepaalde studie gefokus word. 'n Werksvloei met die doel om die maksimum voordeel uit hierdie tipe prosedures te trek is gekonseptualiseer, wat behels dat die twee chirurgies verwyderde bene gebruik word om die oorblywende geometrie te voorspel deur 'n statisties gevormde model by 'n vormskattingsproses te inkorporeer. 'n Gesimuleerde prosedure gebaseer op een aspek van polsgewrigvervangingschirurgie is ontwerp ten einde 'n vergelyking te kon tref tussen die gebruik van tradisionele navigasiemetodes en dié wat aangevulderealiteit-(AR)-leiding as steun vir chirurgiese navigasie gebruik. Die resultate van hierdie eksperiment dui op geringe mindere akkuraatheid in vergelyking met die meer tradisionele fluoroskopiese leiding, 'n vermindering in die tydsverloop van die prosedure, en 'n relatief kort waargenome leerkurwe (intuïtiwiteit) met die gebruik van die AR-leiding. Verder word nóg die pasiënt nóg die chirurg met die AR-navigasiesteun aan skadelike ioniserende stralingsbronne blootgestel. Ter afsluiting is die outeur van mening dat die ARAOS-tegnologie kliniese doeltreffendheid en uitvoerbaarheid vir gebruik in die operasieteater toon met die potensiaal om bestaande

beste praktyke in ortopediese chirurgie te ondersteun en te verbeter en meer bekostigbaar en intuïtief as ander vorms van navigasiesteun te kan wees.

Dedication

I would like to dedicate this thesis to my father, Lex Holmes, who sadly passed away on 31 December 2016.

Acknowledgements

I would like to extend my gratitude to the following people: My supervisor (Mr Johan van der Merwe) and co-supervisor (Dr Dawie van den Heever) for their continued guidance and support throughout, Dr Rudolph Venter from the Advanced Orthopaedic Training Centre at Tygerberg Hospital for his input and expertise from a medical perspective as well as for offering up his time to assist in the experimental process and finally, to both my parents for their support over the years.

Contents

List of Figures

List of Tables

List of Abbreviations

A/P ..... Anterior/posterior
AOTC ..... Advanced orthopaedic training centre
AR ..... Augmented reality
ARAOS ..... Augmented reality-assisted orthopaedic surgery
CAS ..... Computer-assisted surgery
CAOS ..... Computer-assisted orthopaedic surgery
CPD ..... Coherent Point Drift
CT ..... Computerised tomography
DICOM ..... Digital imaging and communications in medicine
DRB ..... Dynamic reference base
EIA ..... Error in insertion angle
EM ..... Expectation maximisation
FOV ..... Field of view
GMM ..... Gaussian mixture model
GPA ..... Generalised Procrustes analysis
HMD ..... Head-mounted display
ICP ..... Iterative Closest Point
MAE ..... Mean absolute error
MRI ..... Magnetic resonance imaging
OR ..... Operating room
OST ..... Optical see-through
PACS ..... Picture archiving and communications system
PCA ..... Principle component analysis
PDM ..... Point distribution model
PVP ..... Percutaneous vertebroplasty
RMSD ..... Root mean square difference
SDK ..... Software development kit
SOTA ..... State-of-the-art
SSM ..... Statistical shape modelling

VIPAR ..... Virtual protractor with augmented reality
VR ..... Virtual reality
VST ..... Video see-through

List of Symbols

$\mathbf{b}$	Vector of model parameters
$\mathbf{b}_y$	Model parameters for best fit full shape approximation
$C(K)$	Compactness as a function of K
D	Sum of distances
$G(K)$	Generality as a function of K
K	Number of retained modes of variation
L	Linear mapping
$M(\mathbf{b})$	Parameterised model
n	Number of points
$\mathbf{n}$	Residual vector
N	Number of model instances
$p(\mathbf{b})$	Distribution of model parameters
s	Number of instances in the training set
$S(K)$	Specificity as a function of K
$\mathbf{S}$	Covariance matrix
t	Number of eigenvectors
x_i, y_i, z_i	Point position vector
$\mathbf{x}$	Shape vector
$\overline{\mathbf{x}}$	Mean shape vector
$\tilde{\mathbf{x}}$	Estimate of full shape vector
$\mathbf{y}$	Partial input observation

η	Regularisation term
λ	Eigenvalue
Λ	Eigenvalue matrix
Φ	Eigenvector matrix
Φ_{t_y}	Predictors component directions
Δy	Centered partial observation

Chapter 1

Introduction

Effectively viewing bony anatomy intraoperatively continues to be a key desire for orthopaedic surgeons. With the emergence of virtual and augmented reality (VR/AR) technology in recent years and with their rapid pace of development, intraoperative 3D visualisation of patient specific anatomical information is now a possibility. This chapter includes background information introducing the reader to important concepts and terminology covered in later chapters, the motivation for pursuing this project as well as the objectives set out for the successful completion thereof. Lastly, a brief overview of each chapter is provided.

1.1 Background

The term "surgical navigation" spans a broad area which, depending on the clinical challenge, may have numerous interpretations. Surgical navigation predominantly refers to the methods and techniques used to locate anatomical targets, how to reach those targets safely, and the position of surgical tools and implants with respect to these targets (Mezger *et al.*, 2013). It also serves as an important measurement and verification tool used by surgeons to evaluate their actions and to assist with decision-making. Surgical navigation has allowed for safer, less-invasive procedures to be carried out. An important prerequisite for being able to navigate intraoperatively was the advent of medical imaging techniques such as X-ray radiography, computerised tomography (CT), magnetic resonance imaging (MRI), fluoroscopy, and medical ultrasonography (ultrasound) which has allowed surgeons to see inside patients without the need for an incision (ClaroNav, 2017).

Computer-assisted surgery (CAS) refers to a set of surgical methods that make use of various computer technologies for surgical planning as well as for guiding and performing surgical interventions. Robotic surgery is synonymous with CAS, however, the term also encompasses image-guided surgery which

makes use of medical imaging techniques such as those mentioned previously to assist with surgical navigation. The application of CAS is observed across numerous medical specialties, however, computer-assisted orthopaedic surgery (CAOS) refers to CAS techniques being applied specifically in the field of orthopaedics. Orthopaedics is the medical specialty that focuses on the injuries and diseases of the body's musculoskeletal system which includes your bones, joints, ligaments, tendons and nerves.

A relatively recent addition to the category of CAS is that of medical augmented reality. Augmented reality is a display technique which combines real and virtual worlds (Lamata *et al.*, 2010). It allows for preoperative planning information and digital images to be overlaid into the surgeon's field of view (FOV), essentially providing surgeons with a "X-ray vision"-like experience without the need for continuous use of ionising radiation (Figure 1.1).

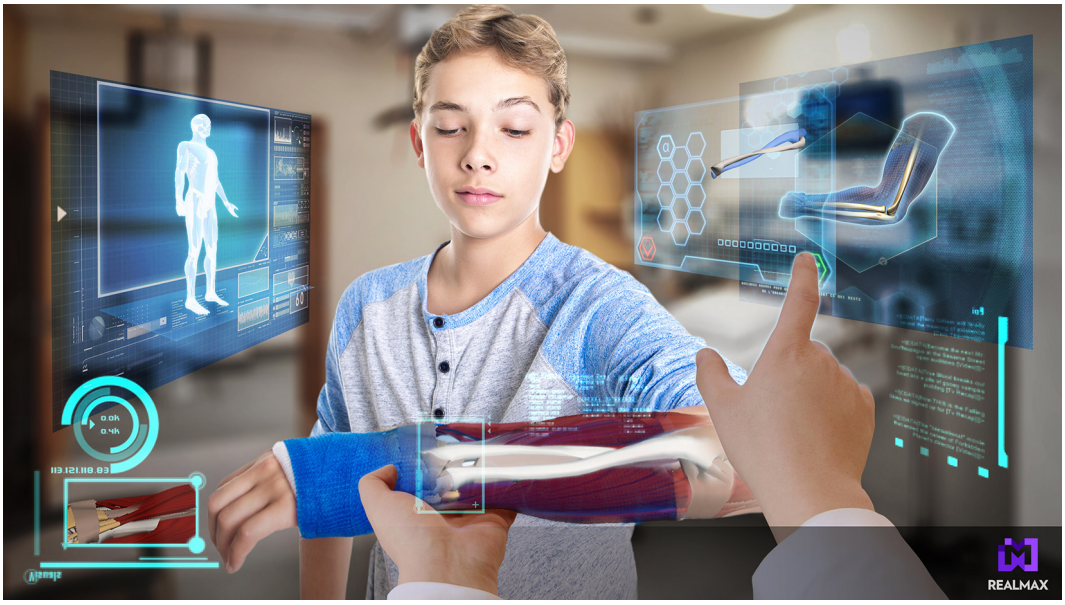

Figure 1.1: Augmented view of otherwise obstructed geometry (Image: Medicalexpo.com, 2017).

1.2 Motivation

The use of CAOS systems is becoming a common method of treatment across the field of orthopaedics. These devices have shown to reduce the variability in implant placement, increase the accuracy of surgical procedures and have shown potential to improve patient outcomes in general. The success of these devices largely depends on the degree to which surgeons understand how they operate as well as their associated limitations or pitfalls (Langlotz, 2004). Of-

ten these devices require extensive retraining in order to operate them safely. This may result in the very procedure during which the device is meant to assist, needing to be altered. Rather than being disruptive, a CAOS system should ideally supplement current best practices followed by surgeons in the operating room (OR). Other pitfalls facing existing CAOS include their bulkiness, being cumbersome to set up and use and the prohibitive costs involved with acquiring such equipment and training medical personnel to operate them. Due to the associated costs, the use of these systems can sometimes be limited to private hospitals and medical care facilities. This is of particular concern in South Africa and other developing countries where access to basic healthcare may be limited and the use of state-of-the-art (SOTA) CAS systems not as widespread as that seen in more developed nations.

Augmented reality-assisted orthopaedic surgery (ARAOS) has the potential to improve accuracy during surgical navigation irrespective of what particular procedure is being carried out. The use of AR may facilitate better placement of instruments, guides, jigs, tools and implants while being more intuitive than other forms of CAOS (Nikou *et al.*, 2000). An ARAOS system, while based on SOTA technology, is not overly complicated and could require minimal additional training to prove useful in the OR. The ideal implementation of ARAOS could be centered around the use of mobile technology which makes use of a cellular smartphone placed in a head-mounted display (HMD) allowing the surgeon to visualise the anatomical target within his/her FOV, and thus focus is kept on the patient at all times.

Mobile AR is rapidly becoming more widespread, access to which is essentially available to anyone with a smartphone or tablet. With such ease of access, along with factors such as being more compact, less expensive, and more intuitive to operate, ARAOS has the potential to have a significant cost-to-impact ratio in the OR. This is particularly attractive for use in the developing world. The hardware itself (consisting of a smartphone and an HMD), would be procedure independent, which is another major advantage over other CAOS systems, and allows for AR applications to be developed tailored to a particular procedure. Smartphone-based AR navigation systems also provide opportunities for use in telemedicine and remote teaching.

AR technology, although a relatively recent addition to a surgeon's toolbox, is developing at a rapid pace with improvements being made with respect to image registration and tracking (Okamoto *et al.*, 2014). These technical aspects are also the areas best covered in literature (Shuhaiber, 2004). There appears, however, to be a sparsity of studies relating to the overall feasibility of AR technology in the OR, evaluation of the constituent subsystems in a clinical setting as well as the evaluation of improvements in terms of surgical outcomes (Kersten-Oertel *et al.*, 2013). Prohibitive costs and difficulties

associated with implementing such studies on actual patients (e.g. obtaining ethical clearance, time limitations, gaining access to the technology) is most likely to blame for the lack of studies pertaining to the use of medical AR. It is these aforementioned deficiencies that this study aims to address.

1.3 Aims and objectives

The aim of this study is to investigate the clinical efficacy and feasibility of an application of ARAOS technology that focuses on supporting and enhancing current best practices in orthopaedic surgery. The specific objectives set out towards successfully achieving this are:

1. Through consultation with an orthopaedic surgeon, identifying a clinical problem most suited to an initial proof-of-concept approach,
2. conceptualising a procedural workflow aimed at providing streamlined and affordable intraoperative navigational assistance,
3. development of a mobile, smartphone-based ARAOS application, and finally,
4. validating its effectiveness *in vitro*.

1.4 Structure of document

Chapter 2: This chapter includes a literature review pertaining to surgical navigation in a broad sense, its inception with the first applications centered around neurosurgery and stereotaxy, the importance of medical imaging in surgical navigation, its evolution over the years, as well as the basic principles behind a typical surgical navigation system. Navigation specifically in the field of orthopaedics is then discussed as well as the drawbacks and limitations of current orthopaedic navigation systems. Next, an introduction to ARAOS is given together with an overview of a typical AR system and the current trends in AR technology. Lastly, two case studies involving the use of AR to assist with navigation in orthopaedic surgery are included.

Chapter 3: This chapter discusses the methodology followed in order to achieve the stated aims and objectives outlined in Chapter 1. Firstly, the clinical problem chosen for this study is discussed together with a breakdown of the relevant anatomy. Next, the surgical technique used and procedural workflow followed is given with emphasis placed on one particular prosthetic implant as an example. Furthermore, the conceptual procedural workflow under AR assistance is proposed which includes utilising Statistical Shape

Modelling (SSM) to estimate obscured anatomy based on a partial or sparse input. A brief introduction to SSM is provided followed by the underlying theory. The methods used in this study to obtain this partial input are then given as well as how these methods will be evaluated in terms of their accuracy. Lastly, an outline of a simple experiment based around the selected clinical problem and aimed at simulating a potential augmented reality (AR)-guided procedure is given.

Chapter 4: This chapter begins by presenting the results from the validation of the SSM. Next, results pertaining to the accuracy of the 3D object scanner as well as the custom-built AR-based point digitising application are given. Following this are the results of using these methods to obtain a partial input with which to estimate the full shape vector by incorporating the SSM. Furthermore, the results from the AR concept application and simulated procedure are provided. Completing the chapter are discussions on the various sets of results gathered with reference to existing literature.

Chapter 5: This chapter includes the conclusions drawn from the experimental process with special attention given to addressing how the project aims and objectives set out in Chapter 1 have been met. Recommendations for future studies relating to the tools and techniques used here as well as studies relating to ARAOS in general are also given.

Chapter 2

Literature review: Surgical navigation

Technological advances in the field of surgical navigation continue to transform surgical interventions into safer and less invasive procedures. It has already been mentioned that surgical navigation concerns identifying an anatomical target's location, the methods that will be used to reach that target safely, and the position of an implant or surgical tool with respect to that anatomical target. Furthermore, it is used by surgeons as a measurement tool to verify their actions and to assist with their decision-making. In some cases, the benefits from the introduction of surgical navigation systems have been apparent almost immediately (e.g. the invention of X-ray technology allowing the surgeon to see inside a patient for the first time). This chapter discusses the inception of surgical navigation which includes addressing the first applications of this technology primarily in the field of neurology and intracranial procedures. The principles of surgical navigation are then outlined after which navigation in the field of orthopaedic surgery is discussed. Lastly, the current trends in augmented reality-assisted orthopaedic surgery (ARAOS) and case studies thereof are looked into and a breakdown of the constituent subsystems which typically comprise an augmented reality (AR) device is given. Much of what is discussed in this chapter is covered by work presented by Mezger *et al.* (2013) and Langlotz (2004), however, the most important topics relevant to this particular project are summarised in the following sections.

2.1 The inception of surgical navigation

The first experiments carried out with the goal of precisely locating specific anatomical targets can be traced back to the late nineteenth century (Enchev, 2009). The introduction of medical imaging was an important prerequisite to surgical navigation. Wilhelm Roentgen discovered X-ray technology in 1895

(Nde-ed.org, 2017). This enabled new possibilities with respect to medical diagnosis and treatment and was the first time practitioners could see obscured anatomy inside a patient without the need for an incision. The advancement of medical imaging technology together with the rapid improvement of computer processing capabilities and the presence of a number of pioneering surgeons, was the driving force behind advances in surgical navigation technology (Mezger *et al.*, 2013). Surgeons have continued to push for the development of new technology to solve their surgical challenges and this has enabled for safer, less invasive procedures to be carried out.

2.1.1 Neurosurgery

Initial applications of surgical navigation were centered around neurosurgery. The brain being the most complicated and delicate organ in the human body, technology has played a major role in improving patient outcomes in these procedures. Throughout the history of brain surgery, surgeons have tried to carry out their procedures as minimally invasive as possible to reduce the chance of any trauma occurring on the brain as well as to reduce the likelihood of infection (Mezger *et al.*, 2013; ClaroNav, 2017). Due to the abundance of intricate structures, any such damage can result in significant functional loss for the patient which undermines the degree of success to which a procedure is completed. One significant issue neurosurgeons deal with is operating in a confined space which lacks anatomical landmarks. This makes orientation of any navigational assistance problematic (Seeger and Zentner, 2002; Mezger *et al.*, 2013).

2.1.2 Stereotaxy

Stereotaxy is a neurosurgical procedure in which the exact localisation and targeting of intracranial structures is required for the placement of electrodes, needles, or catheters (Ganz, 2014). At first, planning for these procedures was carried out with assistance from general anatomical drawings or atlases for intracranial target planning and with the help of a mechanical frame fitted onto the patient's skull (Figure 2.1(a)). Once planning was finalised, the target could then be transferred to the actual intraoperative setup involving the patient. With the trajectory now defined, only a blurr hole (i.e. small hole drilled into the skull to relieve pressure from fluid build up on the brain) is then drilled after which a needle or electrode is inserted (Mezger *et al.*, 2013; Neurosurgery.org, 2017; Hopkinsmedicine.org, 2017). This minimises the likelihood of any brain trauma occurring. One issue with this approach is that the anatomical atlas used during the planning process is not patient specific. In other words, it does not account for a patient's individual anatomy. The inherent error with this approach is then further exacerbated in pathological cases such as when a growing tumor is present. With the advent of medical

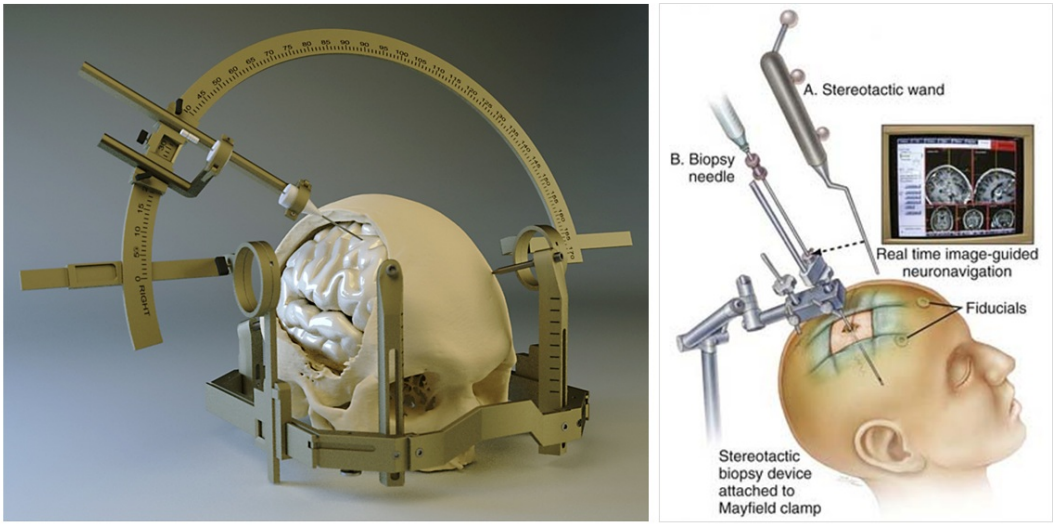

(a) (b)

Figure 2.1: (a) Frame-based stereotaxy (Image: Anon, 2017), (b) frameless stereotaxy (Image: Woodworth *et al.*, n.d.).

imaging technology, patient specific anatomical images could now be obtained and used for stereotactical planning (Orringer *et al.*, 2012; Mezger *et al.*, 2013).

2.1.3 Medical imaging

It was mentioned at the beginning of this chapter that the invention of X-ray technology enabled surgeons to get a glimpse inside patients for the first time. X-rays were initially used in the military to locate bullets in extremities. Thereafter, applications extended to making use of skull radiographs to assist with stereotactic targeting (Nde-ed.org, 2017). The major disadvantage of using X-rays is that they fail to display much detail in terms of intracranial soft tissue (or soft tissue in general) (Diffen.com, 2017). Clinicians pushed to find methods of overcoming this dilemma. Methods such as ventriculography developed by Walter Dandy (Kilgore and Elster, 1995) and pneumoencephalography were experimented with and allowed for better X-ray images of the brain's interior structures. Pneumoencephalography enabled the calculation of stereotactic coordinates for targets within the basal ganglia and thalamus due to their positional relationship to that of the third ventricle (Mezger *et al.*, 2013).

As computer processing capabilities improved, it became possible to reconstruct a 3D image from a set of 2D X-rays. Sir Hounsfield, who is the inventor of the first computerised tomography (CT) device (Imaginis.com, 2017; Impactscan.org, 2017), accomplished just that. CT images allowed for 3D targeting and thus resulted in a significant leap in stereotactic head frame design

(Mezger *et al.*, 2013; Textbook of Stereotactic and Functional Neurosurgery, 2009). These devices proved to be extremely useful and are in fact still in use today. Although CT images remain a valuable tool to neurosurgeons, the introduction of magnetic resonance imaging (MRI) not only allowed for images of soft brain tissue to be captured in detail, but also allowed for the imaging of functional brain areas such as the motoric and speech regions (Radiology-info.org, 2017). Additionally, MRI enabled surgeons to visualise a lesion in relation to other risk structures which offered further assistance in terms of preoperative planning (Mezger *et al.*, 2013).

2.1.4 Evolution from frame-based stereotaxy to frameless navigation

Frame-based stereotaxy had a number of limitations (Grimm *et al.*, 2015; Bic.mni.mcgill.ca, 2017). One such limitation was the fact that only very particular types of procedures involving blurr holes were suitable for this approach. Examples of such procedures are biopsies, electrode placements, and the resection of small intracranial tumors. Other disadvantages of this approach include significant patient discomfort from the time of initial preoperative scanning through to surgery, the inability to visualise the biopsy needle pass, a limited view of the operating area, as well as having no intraoperative control over the stereotactic pathway or awareness of any complications such as a ruptured vessel (Mezger *et al.*, 2013).

In the 1990s David Roberts developed the concept of frameless stereotaxy for neurosurgery to overcome these limitations (Enchev, 2009). Frameless stereotaxy allowed for real-time tracking of surgical instruments and for viewing the current position of these instruments on a preoperatively obtained CT or MRI scan (McInerney and Roberts, 2000; Peters *et al.*, 1994) (Figure 2.1(b)). This was in fact the inception of surgical navigation as we know it today. The introduction of real-time surgical navigation not only allows a surgeon to constantly have an awareness of an anatomical target's location, potential risk areas, intraoperative orientation, but also supports optimal implant placement and can serve as an important measurement tool to assist with intraoperative decision-making (Mezger *et al.*, 2013).

The introduction and integration of technology such as medical imaging and stereotaxy has driven the evolution of surgical navigation allowing surgeons to carry out ever more effective and less invasive procedures. Surgical navigation is by no means limited for use in neurosurgery and has in fact become common practise in numerous other medical specialties.

2.2 Principles of surgical navigation

A surgical navigation system attempts to determine the position of an object in space with respect to its surroundings. Modern surgical navigation systems make use of stereoscopic cameras which emit infra-red light. This light then reflects off identifiable objects, often referred to as fiducial markers, to determine their 3D position in real-time. In some cases these markers take the form of multiple reflective spheres which are attached to surgical tools or the patient's bony anatomy. Such a setup generally also requires a computer and display, as well as the associated navigational software needed to process the sensor input and to output the current positional information (Mezger *et al.*, 2013; Knowcas.com, 2017) (Figure 2.2).

Figure 2.2: Modern surgical navigation system (Image: MedicalExpo, 2017).

In terms of the fiducial markers, at least three are needed to determine the position and orientation of an object (if reflective spheres are used). It may be necessary to employ more, somewhat redundant markers, to avoid losing tracking ability when one or more markers may be obstructed. The markers attached to the patient (e.g. to a bone) are taken as the reference position and the position of a surgical instrument is then calculated with respect to this

reference. The camera itself can be moved intraoperatively as only the relative position between objects is of interest.

Surgical navigation in neurosurgery and spinal surgery is usually "image-based". This means that imaging data acquired preoperatively (such as CT or MRI images) is used to assist with navigation intraoperatively. During pre-operative planning, these images can be enriched with additional data such as highlighted areas of interest, a surgical path and other forms of navigational assistance (Mezger *et al.*, 2013). Before the procedure can begin, the preoperative imaging data needs to be matched onto its correct position with respect to the patient's actual anatomy. This process is known as image registration. Registration establishes the relationship between the "real" coordinate system defined by the reference array attached to the patient and the "virtual" coordinate system of the imaging data (Wyawahare *et al.*, 2009). Registration can be accomplished in a number of ways such as paired point-based registration or the use of surface matching routines (Mezger *et al.*, 2013). Further images can be acquired intraoperatively and again registered onto their correct anatomical position and orientation.

In orthopaedics, surgical navigation is usually "model-based" and is accomplished almost entirely without information from external image sources. The advantage of this approach is that patients are not continually exposed to radiation sources such as X-ray or CT. The navigation software calculates an individual model of the patient's anatomy based on predefined landmarks present on a bone which are acquired using a navigated instrument. This model can then be used to preoperatively plan the position and orientation of an implant after which the combined information is used for navigating intraoperatively (Mezger *et al.*, 2013).

Although navigation for neuro-, spine and orthopaedic surgery has been mentioned, each surgical discipline has its own requirements. Additionally, each hospital or individual surgeon may have different navigational preferences for their particular workflow. Some situations may be extremely specific whereas others may require a certain degree of flexibility and functionality. Surgical navigation systems may be semi-permanent installations within the operating room (OR) or sometimes take the form of mobile platforms which can be transported easily and used in several ORs at different times providing further flexibility.

2.3 Navigation in orthopaedic surgery

In orthopaedics, despite the fact that every patient is unique, the intraoperative workflow across procedures is generally similar. For instance, in joint replacement the goal is to replace the joint with an implant that reproduces

the patient's natural geometry as best as possible and to place it in its correct position and orientation (biomechanical alignment) precisely and accurately (Mezger *et al.*, 2013; Langlotz, 2004). Therefore in orthopaedic surgery, it is satisfactory to have a precise measurement tool only. Surgeons often extrapolate from what they can see to make an "educated guess" with regards to the location of high risk anatomy. This is in contrast to neurosurgery where the primary goal is to obtain precise localisation of risk areas such that they can be avoided. The aim of navigation in joint replacement is to make these procedures more accurate and reproducible (Jaramaz *et al.*, 1998; Schep *et al.*, 2003). Most joint replacement procedures are carried out at "normal" health care facilities rather than specialised institutions (i.e. medical institutions able to provide rare expertise, certain equipment etc.). In order to be as beneficial as possible, any navigation system must aim to satisfy the expectations of the user, it should be able to be integrated into the OR seamlessly without disrupting the conventional surgical workflow and come at minimal additional cost and effort.

2.4 Current orthopaedic navigation systems and their associated limitations

2.4.1 General aspects of surgical navigation

There are certain drawbacks and limitations with regards to current orthopaedic navigation systems which prevent their widespread use (Blakeney *et al.*, 2011; Lehnen *et al.*, 2010). There is still room for improvement with regards to their usability and it is often the case that surgeons need to go through a learning curve for each procedure which requires navigation. The role of these systems should be to supplement the normal course of action taken in the OR rather than being an obstacle (Rivkin *et al.*, 2009). Often these systems are bulky and cumbersome to set up and use. They generally require a certain degree of hand-eye coordination from the operator and at times the operator may have to view for instance, a computer screen, that may be out of the surgical field of view (FOV), therefore intermittently taking focus off the patient or operating site. There are systems available now that have a computer screen attached to the actual surgical instrument allowing the surgeon to keep focus on the operating site (Figure 2.3). Products are continually being streamlined to become more intuitive and more in line with what surgeons actually require. In general, for each new procedure careful thought must be given to the placement of the navigation system in combination with other equipment present within the OR (Langlotz, 2004).

It has already been mentioned that surgical navigation requires the tracking of surgical instruments and anatomical structures and that this is usually accom-

Figure 2.3: Use of Brainlab Dash navigation system during total knee replacement surgery (Image: Mezger *et al.*, 2013).

plished by making use of an optical tracking system. These optical tracking systems generally take the form of infra-red light emitting diodes or infra-red light reflecting spheres. In order to track these objects, the camera is required to have a direct line of sight of them. Unfortunately this is not always simple to achieve and careful thought must be given to the placement of a camera system within the OR. This largely depends on the available space, the position of medical personnel around the operating table, the personal preferences of the surgeon, and possibly the cable lengths between subcomponents of the navigation system (Koivukangas *et al.*, 2013; Birkfellner *et al.*, 2008) (Figure 2.4). Additionally, optical tracking systems usually have an optimal distance at which they perform best. A further complication is that other light sources (e.g. operating lights or light from a microscope) may interfere with optical tracking systems and thus facing the camera directly at these intense light sources should be avoided(Langlotz, 2004).

A dynamic reference base (DRB) (Nolte *et al.*, 1996) is the term used for the set of reference markers attached to a bone. It is critical that the DRB is fixed to the bone in a stable manner such that it does not shift position at any point leading up to, and during the surgical procedure. Should there be any doubt as to the reliability in the position of the DRB at any time, this must be verified and corrected immediately. If there are any discrepancies between the tracked DRB position and its actual position this may introduce error. This registration issue also applies to surgical instruments being tracked. With the tracking of surgical instruments, the rigid body principle is applied, i.e. each tracked instrument is assumed to be non-deformable. Unfortunately this may

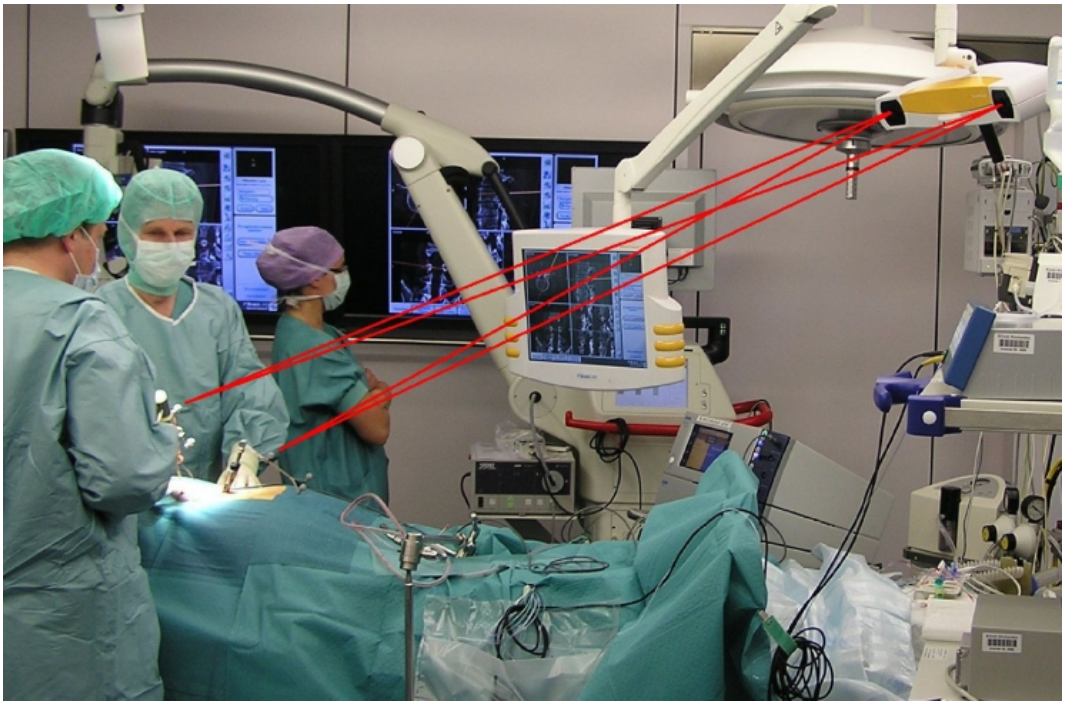

Figure 2.4: Common surgical navigation seen in the OR consisting of a stereoscopic camera (upper right corner) and a computer screen (center). Marker spheres are rigidly attached via a reference array to the patient and to surgical instruments (Image: Mezger *et al.*, 2013).

not always hold true especially for cases in which slim-bodied instruments are used such as thin drill bits or K-wires (Kirschner wires - sharpened and smooth stainless steel pins used in orthopaedic surgery - Radiopaedia.org, 2017) which may tend to bend. There are, however, ways in which the surgeon can compensate for this effect (e.g. anticipation based on experience, incorporating an "error zone" or tolerance, determining deformation and accounting for it, verification via intraoperative imaging). Another issue which is sometimes observed for instruments that are tracked via reflective marker spheres is when one or more spheres become partially or fully obscured by some obstacle in the line of sight between the camera and the object being tracked. Markers can also become covered in for instance, blood, which will obscure the tracking process (Langlotz, 2004). Hence the use of additional, redundant markers may decrease the likelihood of this occurring and increase the reliability and robustness of the tracking system.

One of the most hindering aspects for the widespread use of surgical navigation systems and CAS in orthopaedics is that of the overall cost associated with such systems. Surgical navigation is also a relatively new addition to the field of orthopaedics and thus long-term results proving the benefits (including aspects such as acquisition and training costs, set up and procedural times,

versatility etc.) of its use are not readily available (Langlotz, 2004). Currently however, there does appear to be sufficient evidence to suggest that surgical navigation can contribute to improved accuracy of surgical procedures which inherently lowers the chances of post-procedure complications occurring (Laine *et al.*, 2000). In order to be truly successful in the OR, the benefits achieved by employing computer-assisted orthopaedic surgery (CAOS) systems need to outweigh the often extravagant financial and logistical expenses associated with such technology when compared to more conventional treatment. There are a number of surgical navigation techniques employed in orthopaedic surgery such as CT-based, fluoroscopy-based, and image-free surgical navigation. Each technique comes with its own advantages and drawbacks. A brief overview of each technique is now given.

2.4.2 CT-based surgical navigation

CT-based navigation systems (Figure 2.5) make use of preoperatively acquired CT-scans to assist with navigation. Scanning protocols are usually mandatory for the acquisition of CT images. The Digital Imaging and Communications in Medicine (DICOM) and the Picture Archive and Communication Systems (PACS) allows for easy data exchange between the CT scanner and the navigation system (SearchHealthIT, 2017). CT-based navigation relies on three assumptions. The first assumption is that the preoperative images reflect the intraoperative situation precisely. The second assumption is that the image data correlates with the operated bone with a suffiient degree of accuracy. Lastly, it is assumed that this correlation is maintained from the time of image acquisition and throughout the surgical procedure (Langlotz, 2004). Knowing the degree to which these three assumptions are met is not always clear, however, the operating surgeon is always responsible for judging the trustworthiness of the navigational information being relayed.

The process of image registration is crucial to the success of CT-based navigation systems (Maintz *et al.*, 1998). Registration involves finding the correlation between the image space and that of the patient's actual anatomy. The success of this process largely depends on the quality of the preoperative preparation of the image data. The two most common methods employed to establish correlation is that of paired-points registration and surface-based registration, both of which require preoperative planning (Lavallee, 1996). Paired-points registration also relies on intraoperative identification of preoperatively determined landmarks. These predetermined landmarks must be accessible during surgery and easily identifiable. Registration methods often employ a numeric measure to quantify the quality of the registration achieved with a smaller value indicating better correspondence between image and patient. Inaccuracies associated with registration can be minimised by carefully carrying out the preoperative steps and preparation of imaging data (Langlotz, 2004). Correct

Figure 2.5: Intraoperative imaging of the future with a portable, multi-slice CT scanner tightly integrated with a navigation system for intraoperative use (Image: Copyright: Brainlab AG).

segmentation of CT scans is a prerequisite for satisfactory intraoperative registration as poor segmentation might result in bony landmark features appearing less prominent.

2.4.3 Fluoroscopy-based surgical navigation

The advantage of fluoroscopy-based navigation over CT-based navigation in CAOS is that images are acquired intraoperatively and therefore reflect the current situation (Hofstetter *et al.*, 1997). However, due to the images being acquired intraoperatively there is no possibility to apply computer-aided preoperative planning information to them. With fluorosc-opy-based navigation systems, no manual matching between virtual images and the patient's actual anatomy is required and registration is ensured through calibration of the C-arm or fluoroscope (Hofstetter *et al.*, 1999). Any inaccuracies in the calibration procedure of the fluoroscope is unfavorable and will result in errors being introduced.

Fluoroscopy-based navigation systems generally utilise 2-dimensional C-arms (Figure 2.6) which produce projective images and do not provide a sense of

Figure 2.6: Fluoroscopy-based navigation system (Image: MedicalExpo, 2017).

depth due to the absence of a third dimension, i.e. this form of navigation projects the position of surgical tools in the 2D imaging plane only. The device would have to be rotated perpendicular to the first imaging plane to obtain a second image so as to get an idea of depth in the third dimension. This is what is referred to as the multi-image feature of fluoroscopy-based navigation systems. All that this implies is that tracking or positional information is provided in different planes by making use of previously acquired C-arm images (Langlotz, 2004). Recent developments in C-arm technology has resulted in a new generation of devices capable of generating a 3D dataset from 2D images acquired from numerous viewpoints (Heiland *et al.*, 2003). The acquisition process of these systems does however take several minutes to complete (Rock *et al.*, 2001). Another drawback of this type of 3D navigation system is that it relies on having the patient remain motionless during image acquisition.

For both 2D and 3D fluoroscopy-based navigation systems, the images display the current situation. Any intraoperative manipulation of the patient's anatomy will result in the previously acquired images becoming void, i.e. not the correct representation of the current situation, and thus new images will need to be acquired. Importantly, fluoroscopy-based navigation systems do expose both the patient and the staff in the OR to ionising radiation therefore any unnecessary use of these devices should be avoided.

2.4.4 Image-free surgical navigation

Image-free navigation systems do not incorporate any pre- or intraoperatively obtained image sources. Instead key anatomical features are digitised intra-

operatively by the surgeon and provide sufficient information with which to construct a virtual representation of the patient's anatomy (Dessenne *et al.*, 1995). These methods can make use of statistical models which allow for a full and detailed approximate representation of the patient's anatomy to be generated (Fleute *et al.*, 1999). Image-free surgical navigation does however suffer from a number of pitfalls. Due to the surgeon being solely responsible for accurately generating the initial virtual representation of the surgical scene from which all subsequent navigational feedback is obtained, there is no way to exactly verify that this representation is correct (Langlotz, 2004). One way of obtaining digitised points is by making use of a stylus-like device which is pressed against the bone at a particular position and the surgeon then records this position, repeating with each point digitised. Due to this being a manual process, there is a possibility that a certain degree of error will be introduced.

2.4.5 Conclusion

CAOS systems have the potential to improve a multitude of procedures, however, these are complex systems and can be used incorrectly at times. Any surgeon making use of a CAOS system must understand how it works, how to make use of it correctly, and the associated limitations thereof. Any maloperation of a CAOS system can effect the surgical outcome as well as cause frustration for the operator and prolonged operating times.

2.5 Augmented reality assisted orthopaedic surgery

Augmented reality permits digital images or preoperative planning information to be combined with the surgeon's view of the real world (Blackwell *et al.*, 1998). This technique gives surgeons a "X-ray vision"-like experience without the use of ionising radiation and allows for the visualisation of obscured anatomy which is otherwise not typically exposed during a surgical procedure. Preoperative imaging data can be enriched with further information (e.g. locations of incisions or drill points) and this combined information is then displayed in its correct spatial alignment on the patient. AR has the potential to enable less invasive and minimally invasive surgical techniques to be used which are not technologically feasible at this time (Nikou *et al.*, 2000). Furthermore, AR could provide navigational assistance at a level on par with other more complex CAOS systems while remaining intuitive to use and more affordable than its counterparts.

Previous use of AR in surgery has been somewhat limited. Reasons for this include aspects such as low screen resolution, slow tracking speeds, poor accuracy, and incompatibility of AR systems with the surgical environment. Ad-

vances have begun to make medical applications of AR more feasible and AR systems are on the verge of being used every day in medical training, preoperative planning, preoperative and intraoperative data visualisation, and intraoperative tool guidance (Blackwell *et al.*, 1998). One problem that could be solved by using AR in the OR is that rich medical information is currently available, but often not displayed in the most convenient format. Thus AR could be a viable method of presenting medical information in the best possible way for the surgeon (Nikou *et al.*, 2000).

2.5.1 Augmented reality system overview

AR systems can take on a number of different forms from standalone displays, handheld devices such as tablets and smartphones, to specialised head-mounted displays (HMDs). Currently HMDs usually fall into one of two categories. The first being specialised headsets designed from the ground-up which can either be a non-tethered device with all computing hardware placed on-board the headset itself (e.g. Microsoft Hololens - Figure 2.7(a)) or alternatively take the form of a tethered device which relies on external computing capabilities (desktop or laptop computer) to take care of all processing tasks (e.g. Meta 2 - Figure 2.7(b)). One advantage of utilising a tethered device is that all computing hardware is placed externally. As a result, space is not limited and a more powerful device is likely. Furthermore, tethered devices generally do not have an on-board power supply and as such battery life is at worst limited to that of the external power supply (e.g. laptop's battery). Drawbacks include the presence of cabling and the fact that the device relies upon the capabilities of the external computer which will have to meet the recommended specification for smooth operation.

In terms of non-tethered AR devices, a growing focus is being placed on utilising mobile technology and comprises the second category of HMDs used for AR purposes. Standalone headsets utilising a smartphone for virtual reality (VR) purposes are already widely available (e.g. Google's Cardboard - Figure 2.8(a), Samsung Gear VR - Figure 2.8(b)). Similar technology is now being carried over to AR. Devices such as the Samsung Gear are what is referred to as video see-through (VST) displays. Because the user sees a 2D video image of the real-world, these devices do not provide a sense of depth when required to for instance, use your hands to interact with the real-world. Therefore VST AR devices would not be suitable for continuous intraoperative use within the OR but more likely to be used intermittently. Smartphones with dual depth sensing cameras are starting to be introduced and there is potential for these devices to provide depth perception with a VST display. A better approach to maintain depth perception is to make use of what is known as a optical see-through (OST) display. This type of display projects the augmented scene onto a semi-reflective lens allowing the user to maintain a view of the actual

real world, not a video image of it. Augmented information is then overlaid into the user's real-world FOV therefore maintaining one's natural depth perception.

Figure 2.7: (a) Microft Hololens (Image: Microsoft HoloLens, 2017), (b) Meta 2 (Image: Metavision.com, 2017).

There are OST devices not based around a smartphone such as the Microsoft Hololens and the Meta 2, however, these devices are significantly more expensive than their mobile counterparts. Seebright has recently launched their AR headset semi-equivalent to Google's Cardboard aimed at being simple, affordable and based around smartphone technology. Seebright's Ripple 2 headset (Figure 2.8(c)) which is an OST display can be head-mounted. Ultilising mobile-based AR technology is attractive due to access being available essentially to anyone with a smartphone and therefore promises to be somewhat affordable compared to more specialised AR headsets.

In terms of registering the augmented scene onto the real world, this is usually accomplished by making use of either a set of fudicial markers or an image marker that the camera can track. Image markers contain a relatively dense set of identifiable landmark points within the image and smartphone-based AR

Figure 2.8: (a) Google Cardboard (Image: Store.google.com, 2017), (b) Samsung Gear VR (Image: The Official Samsung Galaxy Site, 2017), (c) Seebright Ripple 2 (Image: Seebright - Developer Kit & Environment for Mixed Reality, 2017).

applications in most cases make use of these types of markers. There are numerous software development kits (SDKs) which make the rapid development of AR applications possible, even for the inexperienced. A popular approach to developing AR applications is to make use of the Unity Game Engine. Unity allows for the import of external AR plugins such as that provided by the Vuforia or ARToolkit SDK.

2.6 Case studies of augmented reality use in orthopaedic surgery

2.6.1 Precision insertion of percutaneous sacroiliac screws using a novel augmented reality-based navigation system: a pilot study

The aim of a study conducted by Wang *et al.* (2015) was to present a novel AR-based navigation system for sacroiliac screw insertion and to evaluate its feasibility and accuracy in cadaveric experiments. Percutaneous sacroiliac screw fixation is a generally accepted and effective method for the treatment of unstable sacroiliac disruption and certain fracture configurations. Compared with open reduction and internal fixation techniques, percutaneous sacroiliac screw fixation is much less invasive with a lower incidence of post-operative wound infection. The traditional method of achieving correct screw placement is to insert it under fluoroscopic guidance, however, multiple views are required, including anteroposterior, lateral, inlet and outlet views, with the surgeon and patient exposed to large amounts of radiation. Moreover, there are inherent errors in fluoroscopic imaging due to factors such as obesity and bowel gas (obesity and bowel gas can obscure visualisation), and these are compounded when images are obtained sequentially in order to cover all four planes (anteroposterior, lateral, inlet and outlet views).

The rates of screw malpositioning are high. Incorrect placement of the sacroiliac screw may cause critical complications, including perforation of the sacral canal, neuroforamina, and iliac vessels. Over the past few decades, various navigation systems were developed capable of facilitating sacroiliac screw insertion, such as 2D fluoroscopy and 3D fluoroscopy, CT-based, and CT-3D-fluoroscopy navigation systems. Compared with traditional techniques, the use of these navigation systems led to an improvement over the number of screw outliers and less radiation exposure.

Six cadavers with intact pelvises were employed in the study. Each cadaver underwent a CT scan whereby the pelvis and surrounding vessels were segmented into 3D models. The ideal trajectory of the sacroiliac screw was planned and represented visually as a cylinder (Figure 2.9). For the intervention, the HMD created a real-time AR environment by superimposing the virtual 3D models onto the surgeon's FOV (Figure 2.10). The screws were drilled into the pelvis as guided by the trajectory represented by the cylinder. Following the intervention, a repeat CT scan was performed to evaluate the accuracy of the system, by assessing the screw positions and the deviations between the planned trajectories and inserted screws.

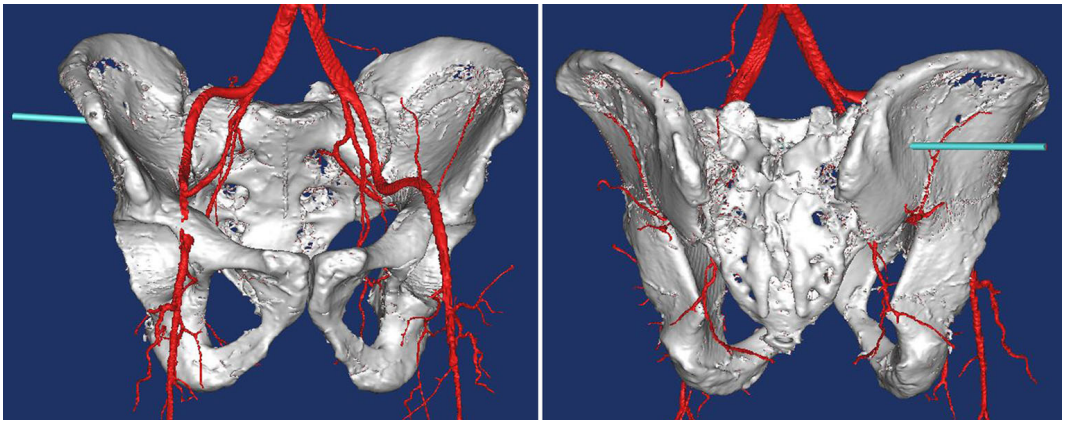

Figure 2.9: Pre-operative 3D reconstruction of the pelvis, planned trajectory, and adjacent vessels (Image: Wang *et al.*, 2015).

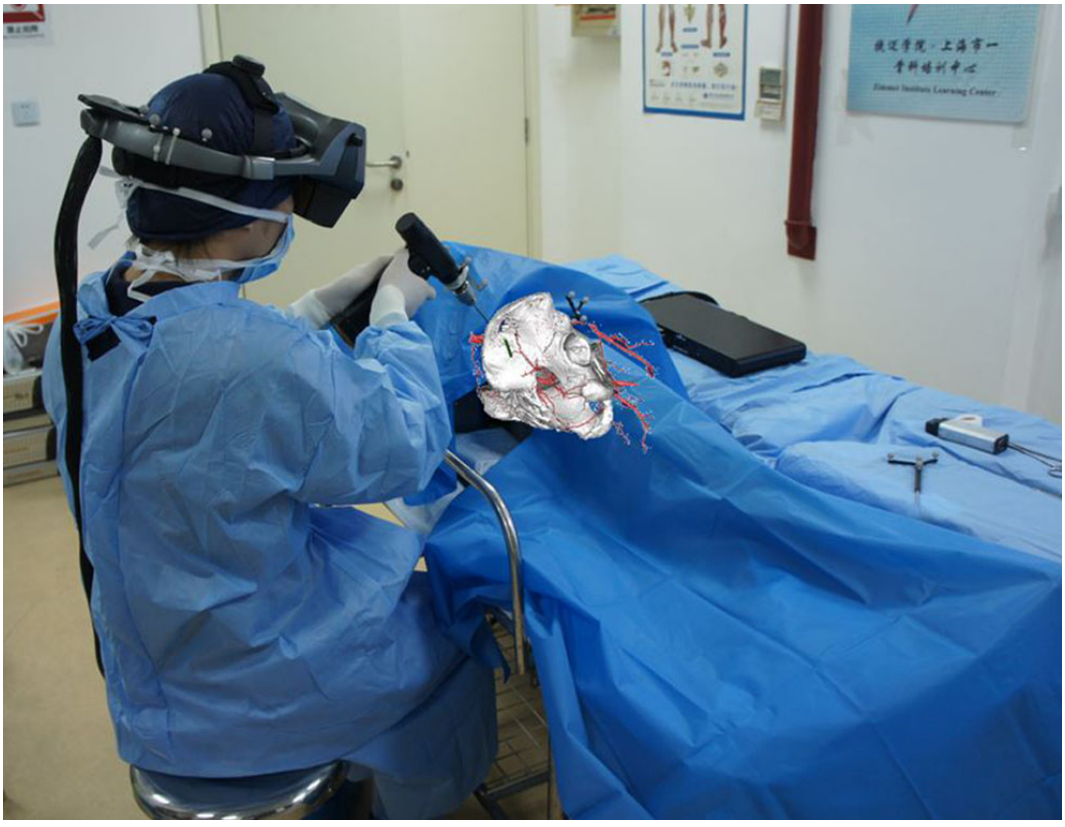

Figure 2.10: Intra-operative drilling under the AR-based navigation with virtual images superimposed on the surgical site through the HMD (Image: Wang *et al.*, 2015).

Post-operative CT images showed that all 12 screws were correctly placed with no perforation. This study suggests an intuitive approach for guiding screw placement by way of AR-based navigation. This approach was found to be accurate and feasible and may serve as a valuable tool for assisting percutaneous sacroiliac screw insertion in live surgery.

2.6.2 A novel 3D guidance system using augmented reality for percutaneous vertebroplasty

This study conducted by Abe *et al.* (2013) aimed to introduce a novel AR guidance system called virtual protractor with augmented reality (VIPAR) to visualise a needle trajectory in 3D space during percutaneous vertebroplasty (PVP). The AR system used for this study comprised a HMD with a tracking camera and a marker sheet. An augmented scene was created by overlaying the preoperatively generated needle trajectory path onto a marker detected on the patient using AR software, thereby providing the surgeon with augmented views in real time through the HMD (Figure 2.11). The accuracy of the system was evaluated by using a computer-generated simulation model in a spine phantom and also evaluated clinically in 5 patients.

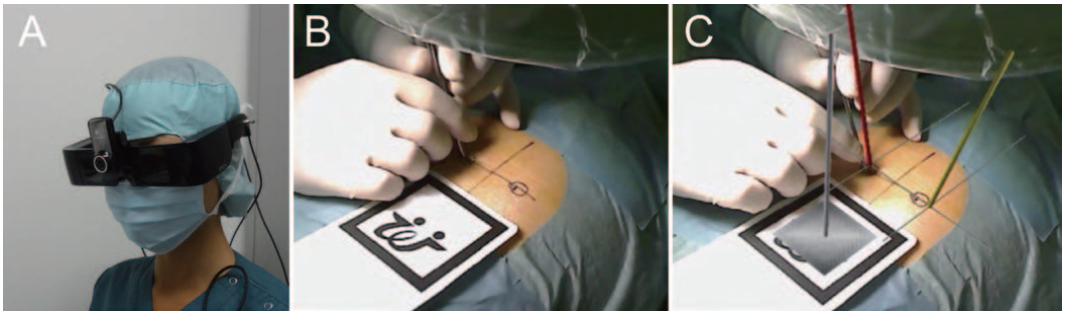

Figure 2.11: Augmented view provided by a video see-through HMD. A: The HMD with a camera. B: Captured raw image of the operative scene by the camera mounted on the HMD. C: Augmented view that the operator actually sees through the HMD (Image: Abe *et al.*, 2013).

In the 40 spine phantom trials, the error of the insertion angle (EIA), defined as the difference between the attempted angle and the actual insertion angle, was evaluated using 3D CT scanning. CT analysis of the 40 spine phantom trials showed that the EIA in the axial plane significantly improved when VIPAR was used compared with when it was not used. The same held true for EIA in the sagittal plane. In the clinical evaluation of the AR system, 5 patients with osteoporotic vertebral fractures underwent VIPAR guided PVP. The postoperative EIA was evaluated using CT. VIPAR was successfully used

to assist in needle insertion during PVP by providing the surgeon with an ideal insertion point and needle trajectory through the HMD. The findings indicate that AR guidance technology can provide assistance during spine surgeries requiring percutaneous procedures.

2.7 Summary

This chapter looked at the inception of surgical navigation, the role that medical imaging played in its advancement, the current trends in surgical navigation technology, the drawbacks of current orthopaedic navigation systems, as well as the potential for AR to assist with surgical navigation during orthopaedic surgery. The use of computer-assisted orthopaedic surgery (CAOS) systems is becoming a common method of treatment across the field of orthopaedics. These devices have shown to reduce the variability in implant placement, increase the accuracy of surgical procedures and have shown potential to improve patient outcomes in general. The success of these devices largely depends on the degree to which surgeons understand how they operate as well as their associated limitations or pitfalls. Rather than being disruptive, a CAOS system should ideally supplement current best practices followed by surgeons in the OR. Other pitfalls facing existing CAOS include their bulkiness, being cumbersome to set up and use, they may require additional training to operate, and the prohibitive costs involved with acquiring such equipment and training medical personnel to operate them.

AR has the potential to improve accuracy during surgical navigation irrespective of what particular procedure is being carried out. The use of AR may facilitate better placement of instruments, guides, jigs, tools and implants while being more intuitive than other forms of CAOS. Furthermore, when combined with "model-based" navigation techniques, image-free navigation may be possible. With these techniques, a reduction in radiation exposure for both the patient and surgeon could result. An ARAOS system, while based on state-of-the-art technology, is not overly complicated and could require minimal additional training to prove useful in the OR.

Chapter 3

Methodology

This chapter discusses the methodology followed in order to achieve the stated aims and objectives outlined in Chapter 1. Firstly, the clinical problem chosen for this study is discussed and was chosen based on a collaborative thought process with a representative from the Advanced Orthopaedic Training Centre (AOTC) located at Tygerberg Hospital. The AOTC forms part of the Division of Orthopaedic Surgery within the Faculty of Medicine and Health Sciences at Stellenbosch University. Next, a brief overview of the relevant anatomy as well as the surgical technique used and procedural workflow followed is outlined with emphasis placed on one particular prosthetic implant as an example. Furthermore, the conceptual procedural workflow under augmented reality (AR) assistance is proposed which forms the basis for the topics discussed later in this chapter. The first of which is that of utilising statistical shape modelling (SSM) to estimate obscured anatomy based on a partial or sparse input. The methods used in this study to obtain this partial input are then given as well as how these methods will be evaluated in terms of their accuracy. Lastly, an outline of a simple experiment aimed at simulating a potential AR-guided procedure is given and will be used in an attempt to evaluate the clinical efficacy and feasibility of using AR to assist with surgical navigation. This experiment may also enable for a comparison to be made with more conventional navigation systems typically used in orthopaedic surgery.

3.1 Identification of a clinical problem

Numerous discussions were held with a representative from the AOTC. The purpose of which was to introduce the idea of using AR to assist with intraoperative navigation for orthopaedic surgery and to identify potential procedures which could be ideal candidates for an initial proof-of-concept study incorporating AR technology. Due to the fact that ethical clearance had already been granted for a separate, non-related study involving the wrist and hand

(Health Research Ethics Committee (HREC) - Ref: S16/01/006), this made for an ideal opportunity to seek out potential clinical problems within this anatomical neighbourhood. It was jointly decided that wrist replacement procedures would make for a suitable candidate as the clinical problem on which focus will be placed for this particular study.

Wrist replacement procedures typically involve partially or fully removing certain bones within the wrist and inserting an articulated wrist joint prosthesis in their place. Indications for these types of procedures include: Rheumatoid arthritis, degenerative arthritis (osteoarthritis), post-traumatic arthritis (secondary arthritis, e.g. failed treatment of intra-articular fractures of the distal radius) (Swemac.com, 2017). Reasons for focusing on this particular procedure include the fact that wrist fractures are amongst the most commonly treated of all fractures (hence the occurrence of post-traumatic arthritis cases) as well as the fact that two bones are essentially removed during these procedures which can be used for shape prediction purposes and potentially allow for scan-free navigation (no radiation exposure). Although a number of prostheses exist for use in these procedures which may differ in design, one such product developed by Swemac will be used as an example to illustrate the intraoperative workflow typically associated with wrist replacement surgery. This wrist prosthesis is currently used in wrist replacement procedures at Tygerberg Hospital. The workflow associated with these procedures is rather involved and therefore the details of which will be kept to a minimum here. However, an overview of the relevant anatomy within the wrist as well as a general outline of the procedure is provided for completeness.

3.1.1 Anatomy of the wrist

The wrist is a complex joint which forms the bridge between the hand and the forearm. In fact, the wrist is not a single joint but is instead comprised of multiple bones and joints each contributing towards the hand's articulation and range of motion (Phillips, 2013). The bones comprising the wrist include the distal ends of the radius and ulna, 8 carpal bones, and the proximal portions of the 5 metacarpal bones (Figure 3.1).

The carpal bones are organised into two groups, a proximal row and a distal row. The proximal row (closest to the distal end of the radius and ulna) includes the scaphoid, lunate, triquetrum, and pisiform (not indicated in Figure 3.1). The proximal row is referred to as a intercalated segment as no tendons are attached to them and their movement is dependent entirely on the mechanical forces from the neighbouring articulations. The distal row of carpal bones is comprised of the trapezium, trapezoid, capitate, and hamate. The distal row articulates with the bases of the 5 metacarpal bones. The bones of the distal row are adherent to each other through the intercarpal ligaments

and these bones are also tightly bound to the metacarpal bones forming what is referred to as the carpometacarpal joint (CMC) (Phillips, 2013; Kijima *et al.*, 2009). Wrist bones of particular interest to this study is that of the third metacarpal, capitate, lunate and scaphoid as these are important with regards to wrist replacement procedures and focus will be placed on these four bones in the discussions which follow.

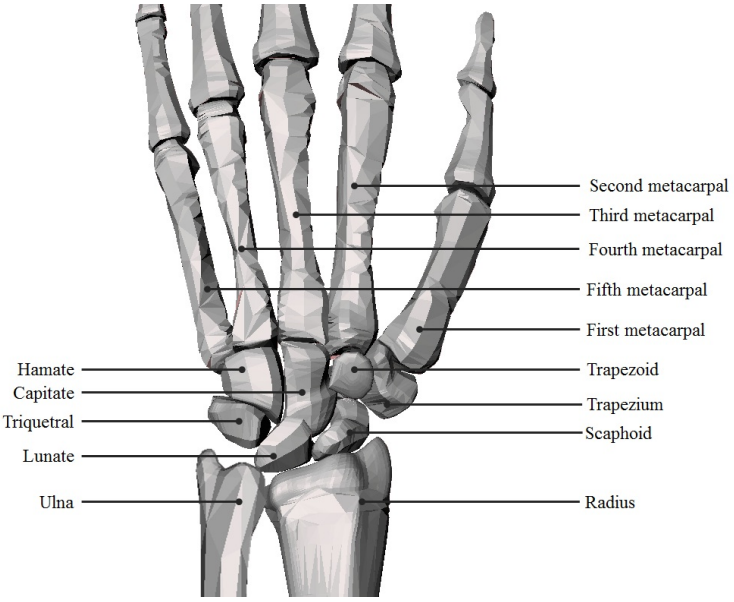

Figure 3.1: Bony anatomy of the wrist.

Briefly in terms of ligaments, the joints of the wrist are surrounded by a fibrous capsule and are held together by an array of ligaments that provide carpal stability. These carpal ligaments can be divided into two groups: intrinsic and extrinsic ligaments. The intrinsic ligaments originate and insert on the carpal bones and extrinsic ligaments form the bridge between the carpal bones and the radius or metacarpals (at their respective ends). This complex array of bones and ligaments provides the hand with 3 degrees of freedom ((1) flexing and extending, (2) pronating and supinating, and (3) deviating ulnarly and radially) and allows for mobility to be maintained without sacrificing stability within the joint (Phillips, 2013; Kijima *et al.*, 2009).

3.1.2 Surgical technique

With the Motec Wrist Prosthesis developed by Swemac, it is advised that the entire lunate and two thirds of the scaphoid are removed (Figure 3.2). The scaphoid segment is removed at a 30 degree angle in order to preserve blood supply, retain the volar ligaments and to prevent any impingement between

the radial styloid and the remaining volar scaphoid (Figure 3.3(a)). It may be preferable by some surgeons to opt to remove the entire scaphoid as the remaining segment can result in impingement and may also limit the range of motion within the wrist post procedure. Moreover, in preparation for the fusion of the third metacarpal and capitate, all subchondral sclerosis and cartilage must be removed at their interface. It is suggested that a 15 degree wedge of bone must be resected to facilitate the alignment of these two bones (Figure 3.3(b)). Careful attention must be given to avoid damaging the volar ligaments.

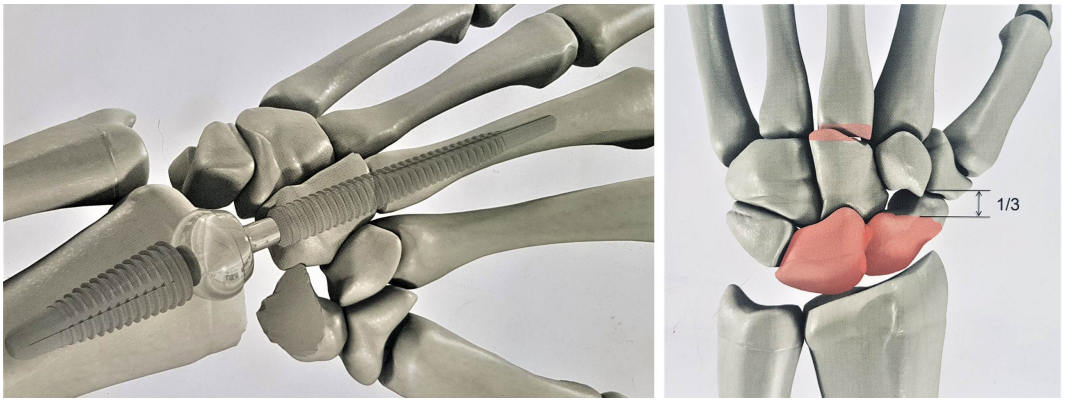

Figure 3.2: Motec Wrist Prosthesis developed by Swemac showing how the entire lunate and two thirds of the scaphoid are removed (Image: Swemac.com, 2017).

Following the preparation of the capitate and third metacarpal, a sharp tip guide wire is inserted through the capitate and about 10-20 mm up the intramedullary canal of the third metacarpal (Figure 3.3(c)). It is important to penetrate the capitate pole at the center or slightly volarly. If penetrated dorsally, there is a risk that the capitate will crack during drilling. Next, the sharp tip guide wire is removed and a blunt tip guide wire is introduced. This time with the guide wire advancing all the way to the distal subchondral bone of the third metacarpal. A blunt guide wire is used to avoid penetrating the cortical wall of the third metacarpal. To ensure proper orientation of the guide wire, it is important that the surgeon have a true anterior/posterior (A/P) and lateral view of the operating site (Figure 3.4(a-b)).

The next step in the process is the drilling of the capitate and third metacarpal. A small diameter drill is introduced over the guide wire and advanced past the isthmus (Figure 3.3(d)). It is important that the threads of the implant engage into the cancellous and cortical bone of the third metacarpal to ensure stable fixation. If no cortical resistance is felt during the drilling process, the drill should be exchanged for a larger diameter drill. Again to ensure proper

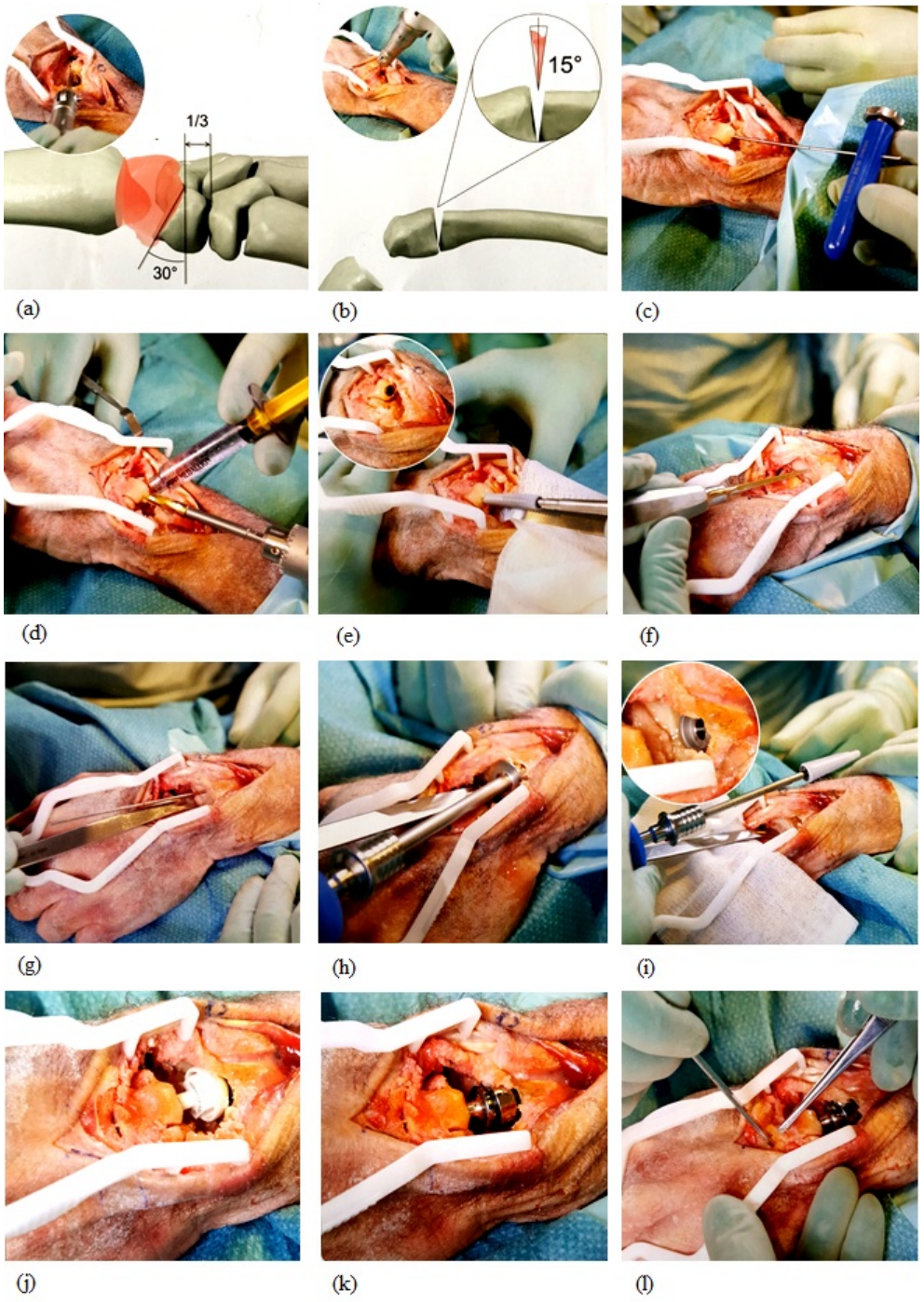

Figure 3.3: Overview of surgical workflow (Image: Swemac.com, 2017).

orientation of the drill, it is important that the surgeon has access to a true A/P and lateral view of the operating site (Figure 3.4(c-d)). Perforating the outer wall of the third metacarpal or fracturing it is a concern should the trajectory of the drill be incorrect. Once drilling is complete, both the guide

wire and drill are removed. Following this, the metacarpal threaded implant can be inserted until its edge is flush with the proximal pole of the capitate (Figure 3.3(e)).

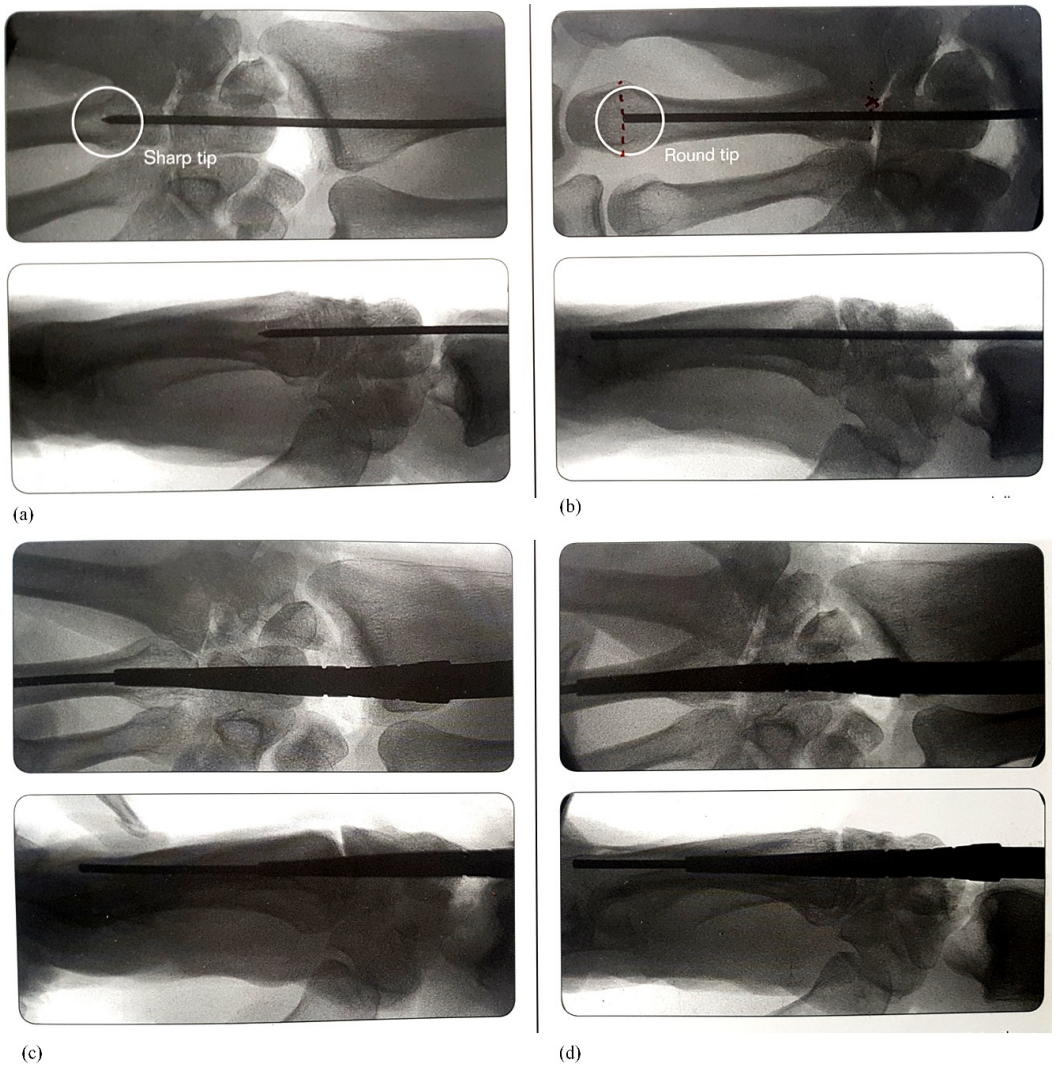

Figure 3.4: A/P and lateral views of operating site to ensure proper orientation of (a-b) guide wire (c-d) small diameter drill.

Now that the capitate-metacarpal end has been taken care of, the next step is to prepare the distal radius for the insertion of its threaded implant. The first step of this process is to insert an awl through the joint surface of the radius (Figure 3.3(f)). Next, a guide wire is inserted through the hole made by the awl and into the radius (Figure 3.3(g)). The orientation of the guide wire is checked through both an A/P and lateral view of the operating site.

A canulated radius drill is then introduced over the guide wire and advanced until cortical resistance is felt. Again, checking for proper orientation. In most cases, the space between the capitate and the surface of the distal radius is not sufficient to allow for the insertion of the prosthesis. In such cases, it may be necessary to ream a cavity for the radius cup to fit into (Figure 3.3(h)). The size of the threaded implant going into the radius needs to be determined and depends not only on the depth drilled but also whether the radius was reamed or not. After this has been determined, the threaded implant is introduced as far as it will go (Figure 3.3(i)).

Next, the radius cup and metacarpal head needs to be sized using trials until the correct tension is achieved (Figure 3.3(j)). After these components have been sized, the actual radius cup and metacarpal head can be correctly placed into their respective threaded implants (Figure 3.3(k)). Once completed, the joint is evaluated for stability and range of motion under image intensification.

To ensure successful fusion of the capitate and the third metacarpal, the gap between these two bones is packed with bone chips gathered during the drilling of the radius, thus improving the likelihood for long term fixation of the metacarpal threaded implant (Figure 3.3(l)). A final reduction of the joint then occurs after which the stability and range of motion is evaluated.

3.1.3 Conceptual procedural workflow under AR assistance

In order to preoperatively visualise a patient's anatomy in 3D, generally the tedious process of segmenting computerised tomography (CT) or magnetic resonance imaging (MRI) scans is required such that a 3D anatomical model can be extracted. Wrist replacement procedures are one particular case in which a 3D model of the anatomy in question could potentially be obtained without the need for a CT or MRI scan.

The concept is to utilise a mobile-based 3D object scanner or 3D point digitiser to digitise points on the surface of the two bones (lunate and scaphoid) which are surgically removed during wrist replacement procedures. These digitised points can then be used as a partial input into a shape estimation algorithm which incorporates a SSM. A SSM describes the variation within a class of shapes and is generated using a training set of shapes obtained from healthy individuals. This allows for an estimate of a patient's geometry to be obtained without the need for a CT or MRI scan. This estimate can then be exported and ideally used in conjunction with an AR device to assist with preoperative planning as well as intraoperative navigation (Figure 3.5).

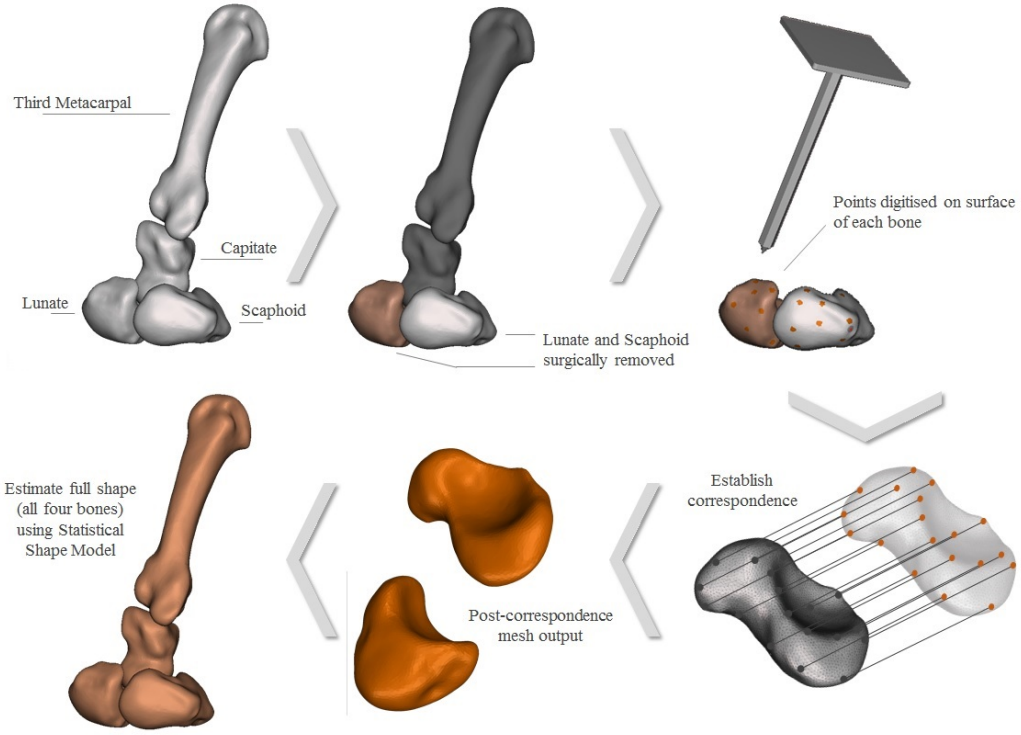

Figure 3.5: Conceptual procedural workflow under AR assistance.

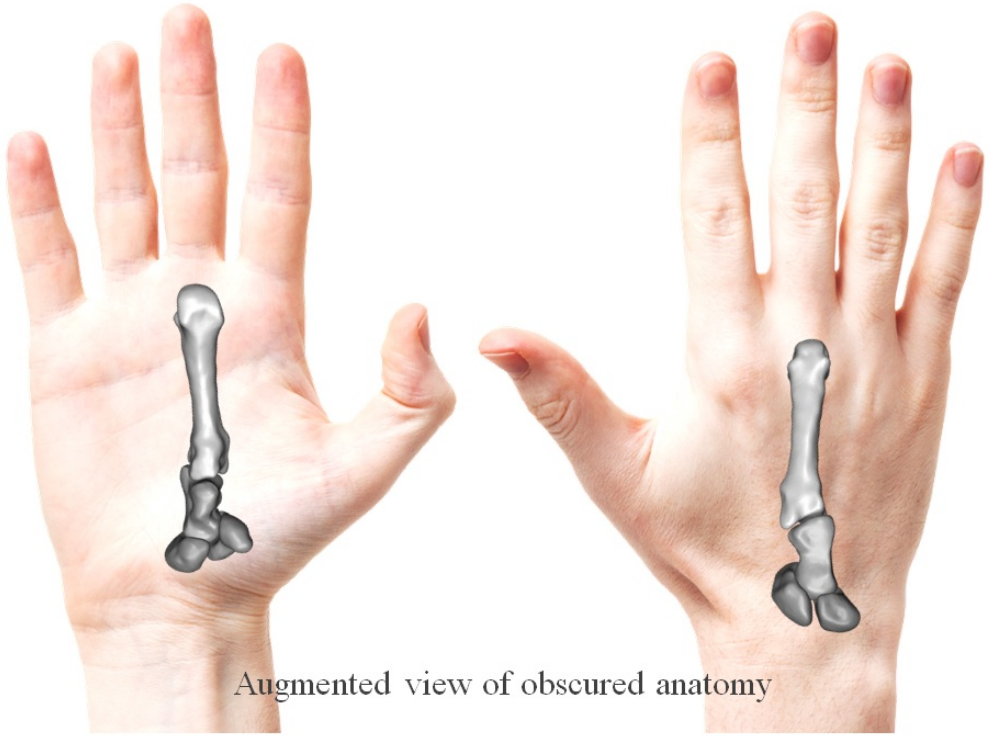

Figure 3.6: Augmented view utilising output from shape estimation process.

The use of AR enables the surgeon to have a continuous intraoperative 3D view of the patient's bony anatomy (Figure 3.6). This will significantly reduce the need for multiple intraoperative fluoroscopic images which expose both the patient and surgeon to radiation. Other potential benefits of this approach include an improvement in surgical accuracy and a decrease in the duration of procedures as well as operating costs.

3.2 Statistical shape modelling

3.2.1 Introduction

Statistical shape analysis (or SSM) is an analysis of the geometrical properties of some given set of shapes by statistical methods. Here statistical shape analysis is carried out using a point distribution model. This implies that a shape is defined by a finite set of coordinate points (e.g. for a 3 dimensional shape, n coordinate points of the form (x_i, y_i, z_i)). If for instance there were s number of similar shapes (all having n number of coordinate points) in the training set, it would be possible to model the distribution of each of the n points in space (hence the term point distribution model).

One of the main methods used in statistical shape analysis is referred to as principle component analysis (PCA). PCA is used to reduce the dimensionality of the shape data to something more manageable. A simple way to visualise what PCA achieves is to envision a cloud of points in 3 dimensions. PCA can be thought of as fitting an ellipsoid tightly over the data where each axis of the ellipsoid is one principle component. If some axis of the ellipsoid is small, this indicates that the variation along that axis is also small, and by omitting that axis and its corresponding principle component from the representation of the dataset, only a relatively small amount of information will be lost (essentially a 3D ellipsoid is modelled by a 2D ellipse). After undertaking PCA on the data, each shape in the training set can be represented approximately using the mean shape plus some component of variation. More details on the topic of PCA are given in Section 3.2.5.

There are a number of preparation steps required in order to perform PCA effectively, the details of which are discussed in Sections 3.2.3, 3.2.4 and 3.2.5. In summary however, there are essentially two requirements in order to conduct PCA. The first requirement is that all shapes are in the same coordinate frame such that only variation in shape is modelled (not variation due to scale and pose), and the second requirement is that points across each training shape correspond (i.e. which point in "point cloud A" is equivalent "point X" in "point cloud B"). The first requirement is met by applying generalised procrustes analysis to the data. This ensures that all shapes in the training set are aligned into a common reference coordinate frame. When using PCA, it is

required that all shapes in the training set have the same number of points (n number of coordinate points). By establishing correspondence between shapes in the training set, this is ensured. There are numerous methods commonly employed to establish correspondence. These preparation steps as well as the steps used in the construction of the shape model are shown in Figure 3.7.

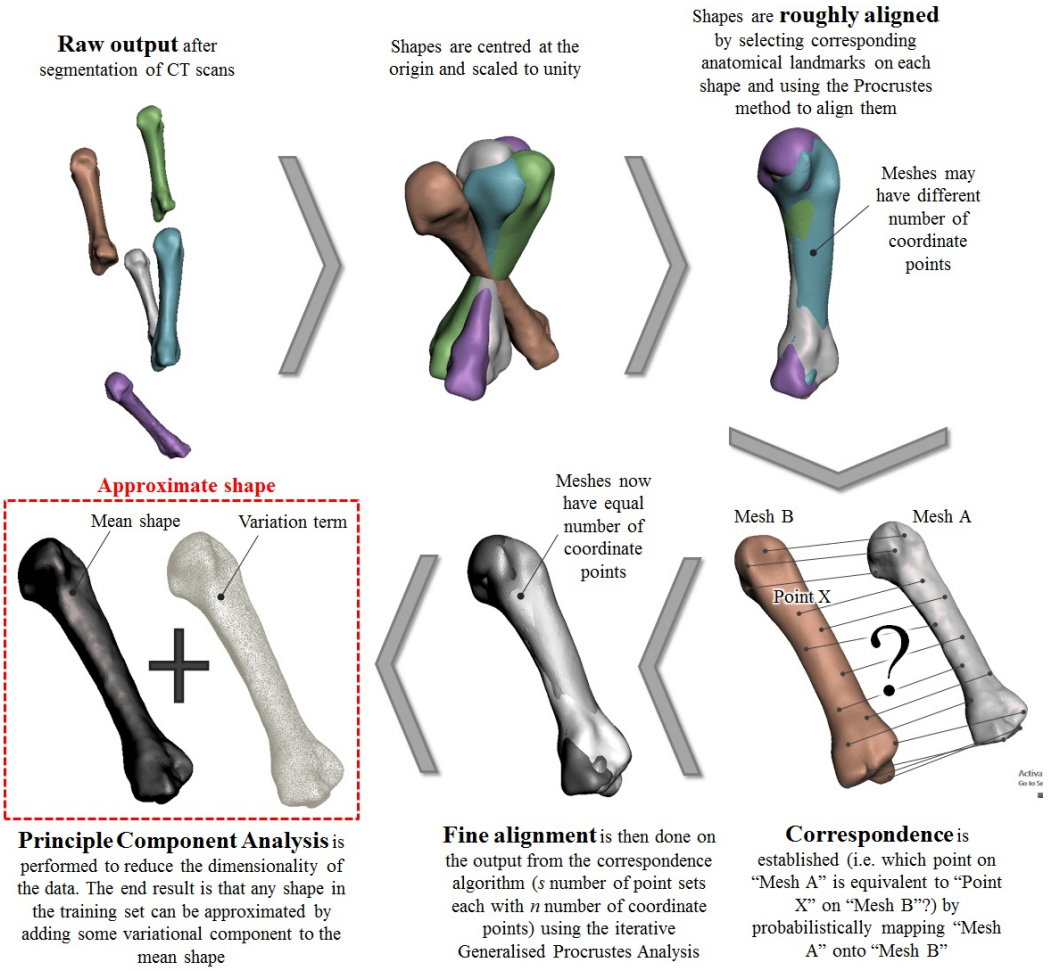

Figure 3.7: Steps involved in the statistical shape modelling process.

3.2.2 Data

Fifty sets of bones (third metacarpal, capitate, lunate and scaphoid) were manually segmented from CT images in order to extract the shapes needed to perform statistical shape analysis. Patients were all adults and for this study it was assumed that any small differences (other than scale) that may be attributable to sex and age were negligible (Crisco *et al.*, 2005). Furthermore, it was assumed that any differences between the left and right hand can be ignored and shapes were mirrored such to all represent the right hand.

3.2.3 Rough alignment

A rough pre-alignment is performed prior to establishing correspondences. This is advised because correspondence algorithms such as the Coherent Point Drift (CPD) and Iterative Closest Point (ICP) algorithms are susceptible to converging to a local optimum if the starting point is too far from the correct registration (Besl and McKay, 1992; Gelfand *et al.*, n.d.; Peng *et al.*, 2016). Rough alignment is accomplished by manually selecting a sparse set of corresponding anatomical landmarks on each training shape and using Procrustes Analysis to align all the training shapes onto a single representative shape. Here landmarks were chosen based on the author's intuition (Figure 3.8). Rough alignment was undertaken for each of the four bones separately.

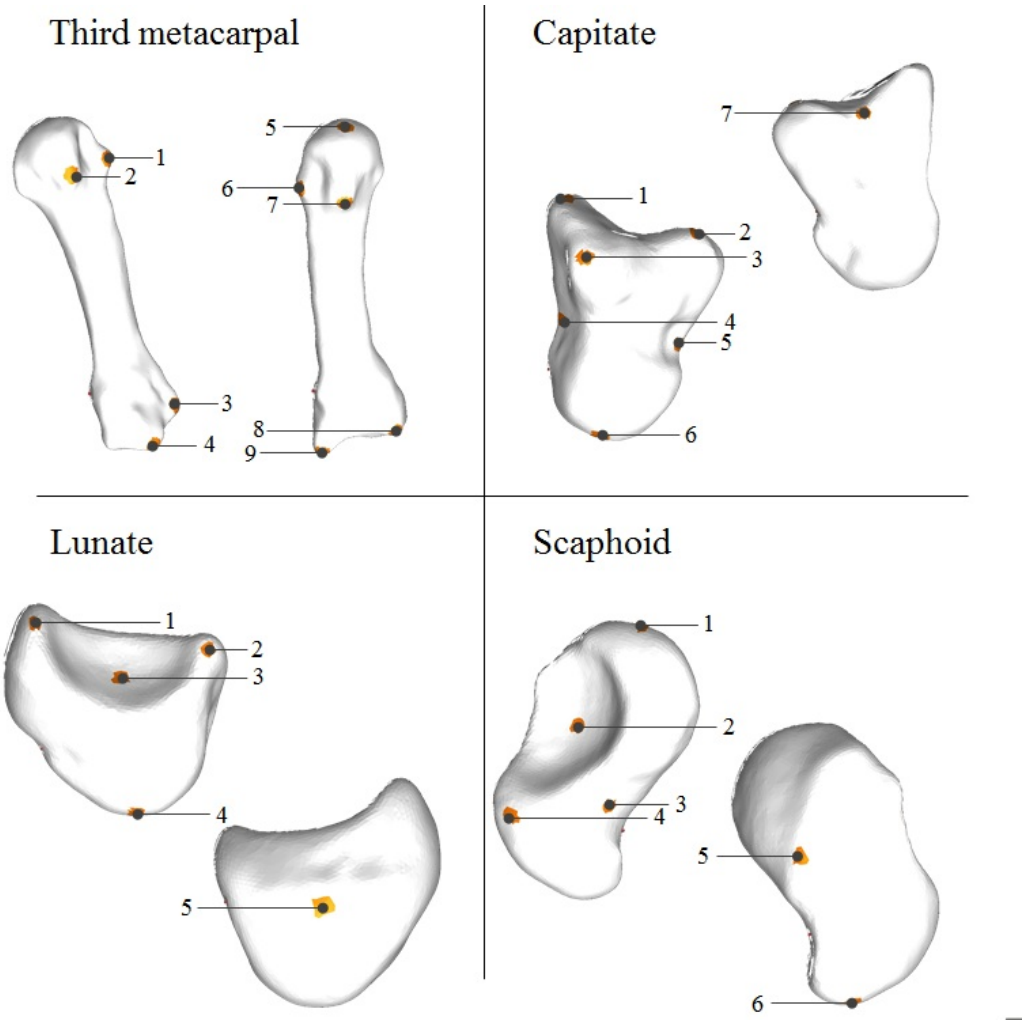

Figure 3.8: Landmark selection for the third metacarpal, capitate, lunate and scaphoid.

3.2.4 Correspondence

A requirement for performing statistical shape analysis using point distribution models (PDMs) is that landmarks on all training shapes be located at corresponding positions (Sarkalkan *et al.*, 2014). The goal of point set registration is to assign correspondences between two dense point sets and to recover the transformation which maps one point set to the other. The point set registration method implemented here is referred to as the Coherent Point Drift algorithm developed by Myronenko and Song (2010).

The CPD algorithm considers the alignment of two point sets as a probability density estimation problem, with one point set representing the gaussian mixture model (GMM) centroids (reference point set) and the other one representing the data points (target point set). At an optimum, the two point sets become aligned by maximising the likelihood of correspondence using the Expectation Maximisation (EM) algorithm. Here the CPD algorithm is used to map a single representative shape onto all other shapes in the training set and the end result is that each training shape has the same number of vertices or landmarks which correspond across all instances in the training set (Figure 3.9). Correspondence was established for each of the four bones separately (third metacarpal, capitate, lunate and scaphoid). The CPD algorithm is later used to find corresponding points present on the 3D-scanned (or digitised) bones and that used in the construction of the SSM.

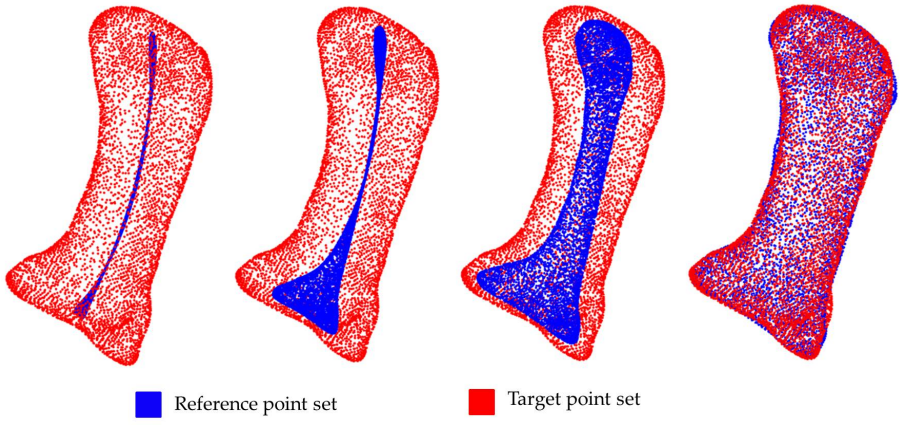

Figure 3.9: CPD algorithm depiction showing the reference point set being mapped onto the target point set.

3.2.5 Shape model construction

Each shape in the training set can, after correspondence has been established, be represented by n points in d dimensions. These points can then be expressed as a nd element vector formed by concatenating the elements of the individual

point position vectors. For instance, in a 3D image we can represent the n landmark points, $\{(x_i, y_i, z_i)\}$, for a single example as the $3n$ element vector, $\mathbf{x}$, where

$$\mathbf{x} = (x_1, ..., x_n, y_1, ..., y_n, z_1, ..., z_n)^T \tag{3.1}$$

Given s training examples, s such vectors $\mathbf{x}_i$ can be constructed. In this case the vertices of each of the four bones were concatenated into a single shape vector. Before statistical analysis can be performed on these vectors it is important that the shapes represented are in the same co-ordinate frame. Shape is defined as a property which is invariant under similarity transformations (Stegmann *et al.*, 2002). Similarity transformations include: Translation, rotation and scaling. Under most circumstances, shape changes induced by these global transformations should not be modelled by a SSM in order to keep the model as specific as possible and therefore should ideally be removed.

A popular method of aligning shapes into a common co-ordinate frame is that of Procrustes Analysis. This approach aligns each shape such that the sum of distances of each shape to the mean ($D = \sum|\mathbf{x}_i - \overline{\mathbf{x}}|^2$) is minimised. Though analytic solutions exist for the alignment of a set, a simple iterative approach referred to as the Generalised Procrustes Analysis (GPA) (Cootes and Taylor, 2001) can be used and is carried out as follows:

1. Arbitrarily choose a reference shape $\mathbf{x}_0$ by selecting it among the available instances in the training set. Scale this reference shape such that $|\mathbf{x}_0| = 1$ and center it at the origin.
2. Superimpose all instances to current reference shape.
3. Compute the mean shape $\overline{\mathbf{x}}$ of the current set of superimposed shapes.
4. Compute the Procrustes distance between the mean shape and the reference shape.
5. If Procrustes distance is less than some threshold, set the new reference shape to the current mean shape. Scale the new reference shape to unity and center it at the origin then return to step 2 until threshold is met.

The result obtained after GPA is a set of s aligned point sets as well as the Procrustes mean, $\overline{\mathbf{x}}$. After alignment, the next step is to reduce the dimensionality of the training set. This involves finding a small set of modes which best describe the observed variation. The set of s aligned vectors $(\mathbf{x})_i$ form a distribution in the nd dimensional space in which they live. If this distribution

can be modelled, it is possible to generate new examples, similar to those in the original training set, as well as estimate new shapes.

A parametrised model of the form $\mathbf{x} = M(\mathbf{b})$ can be constructed, where $\mathbf{b}$ is a vector of model parameters. If the distribution of parameters can be modelled, $p(\mathbf{b})$ then it is possible to limit them such that the generated $\mathbf{x}$'s are similar to those in the training set. PCA is applied to the data set in order to reduce the dimensionality of the data from nd to something more manageable. With the data forming a cloud of points in the nd-s space, PCA computes the main axes of this cloud, allowing one to approximate any of the original points using a model with fewer than nd parameters (Figure 3.10). If Φ contains the t eigenvectors corresponding to the largest eigenvalues, then a member in the training set, $\mathbf{x}$ can be approximated by

$$\mathbf{x} \approx \overline{\mathbf{x}} + \Phi\mathbf{b} \tag{3.2}$$

where $\Phi = (\Phi_1|\Phi_2|...|\Phi_t)$ and $\mathbf{b}$ is a t dimensional vector given by

$$\mathbf{b} = \Phi^T(\mathbf{x} - \overline{\mathbf{x}}) \tag{3.3}$$

The vector $\mathbf{b}$ defines a set of parameters of a deformable model. By varying the elements of $\mathbf{b}$ the shape $\mathbf{x}$ can be varied using Equation 3.2. The variance of the i^{th} parameter, $\mathbf{b}_i$, across the training set is given by λ_i. By applying limits of $\pm 3\sqrt{\lambda_i}$ to the parameter $\mathbf{b}_i$ it is ensured that only legal shape instances similar to those in the original training set are generated. The number of eigenvectors to retain, t, can be chosen such that the model represents some proportion of the total variance of the data or so that the residual terms can be considered to be noise.

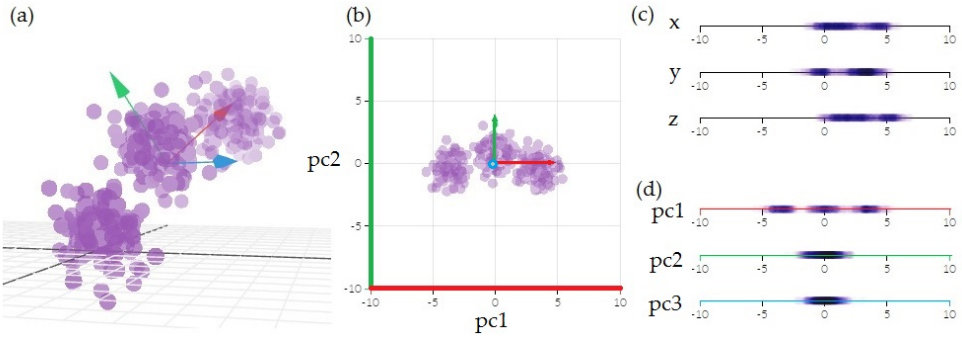

Figure 3.10: Depiction of how PCA is used to reduce the dimensionality of the data. (a) Cloud of 3D points showing three principle component axes, (b) 2D view of the two axes exhibiting the largest amount of variation, (c) distribution of points in x, y and z directions, (d) variation of points along each principle component direction (Image: Explained Visually, 2017).

3.2.6 Shape model validation

The utility of a model depends on its ability to characterise the class of objects modelled (Davies, 2002). Ideally a model should be:

1. General - able to represent any instance of the class
2. Specific - only capable of representing legal instances of the class
3. Compact - with as few parameters as possible

The following formal mathematical definitions for generality, specificity and compactness have been outlined by Su (2011) and Ericsson *et al.* (n.d.). The degree to which a model exhibits generality is obtained using a leave-one-out reconstruction. This involves constructing a model using all but one member of the training set and then fitting this model to the excluded member. This process is repeated excluding each member in turn. The accuracy to which the model can describe the unseen example is measured based on the root mean square distance (RMSD) between the two sets of points. This RMSD is averaged over all turns to obtain the mean squared error, *G(K)* as a function of the number of retained modes of variation, K:

$$G(K) = \frac{1}{s}\sum_{l=1}^{s} RMSD(\tilde{\mathbf{x}}_l, \mathbf{x}_l) \tag{3.4}$$

Here s is the total number of instances in the training set and $\tilde{\mathbf{x}}_l$ is the model instance fitted to the left out member $\mathbf{x}_l$. This model instance is generated using K principle modes and obtained in a similar fashion to the method used in the estimation problem (Section 3.2.7) except with the definition of L now becoming trivial. The standard error of the $G(K)$ mean with standard deviation σ is given by:

$$\sigma_G(K) = \frac{\sigma}{\sqrt{s-1}} \tag{3.5}$$

A specific model is one which only generates instances of the object class which are similar to those in the training set. The quantitative measure of specificity is obtained by generating N number of random model instances with parameters limited within the range of $b_i \in [-3\sqrt{\lambda_i}, 3\sqrt{\lambda_i}]$. The RMSD between the shape in the training set closest to each of the randomly generated model instances is then calculated and averaged over the N number of model instances to obtain specificity *S(K)*:

$$S(K) = \frac{1}{N}\sum_{l=1}^{N} RMSD(\tilde{\mathbf{x}}_l, \acute{\mathbf{x}}_l) \tag{3.6}$$

Again s is the total number of members in the training set, $\tilde{\mathbf{x}}_l$ represents each of the N randomly generated model instances with parameters $b_i \in [-3\sqrt{\lambda_i}, 3\sqrt{\lambda_i}]$. The shape $\acute{\mathbf{x}}_l$ is the nearest member of the training set to $\tilde{\mathbf{x}}_l$. The standard error of $S(K)$ with standard deviation σ is given by:

$$\sigma_S(K) = \frac{\sigma}{\sqrt{N-1}} \tag{3.7}$$

A compact model is one that contains little variance and requires as few parameters as possible to model a shape instance. The compactness measure, *C(K)* is described by the cumulative variance or cumulative sum of the retained K number of eigenvalues:

$$C(K) = \sum_{i=1}^{K} \lambda_i \tag{3.8}$$

Here λ_i is the i^{th} eigenvalue measuring the variance of the data in the i^{th} direction and $C(K)$ is the cumulative variance of the K^{th} mode. The standard error for compactness is defined as:

$$\sigma_c(K) = \sum_{i=1}^{K} \sqrt{\frac{2}{s}}\lambda_i \tag{3.9}$$

Again s is the total number of instances in the training set. Improvement in generality, specificity and compactness for a particular model is indicated with comparatively lower values of *G(K)*, *S(K)* and *C(K)*, respectively.

3.2.7 Shape estimation

Following Blanz *et al.* (2004), a partial but intact input observation $\mathbf{y}$, can be described by

$$\mathbf{y} = L\tilde{\mathbf{x}} + \boldsymbol{n} \tag{3.10}$$

where $\tilde{\mathbf{x}}$ is an estimation of the full shape vector, L is a linear mapping applied to the full shape vector and $\boldsymbol{n}$ is the residual. The linear mapping L is applied to each column of the eigenvector matrix such to obtain the predictor's component directions Φ_{t_y}. The model parameters $\mathbf{b}_y$ for the best fit full shape vector approximation are obtained by solving the least squares optimisation problem (Blanc *et al.*, 2009):

$$\mathbf{b}_y = \arg\min(||\Phi_{t_y}\mathbf{b} - \Delta\mathbf{y}||) + \eta\mathbf{b}^T\Lambda^{-1}\mathbf{b})$$

$$= (\Phi_{t_y}^T\Phi_{t_y} + \eta\Lambda^{-1})^{-1}\Phi_{t_y}^T\Delta\mathbf{y} \tag{3.11}$$

Here $\Delta\mathbf{y}$ is the centered partial observation ($\mathbf{y}$-$L\overline{\mathbf{x}}$). The mapping L consists of ones and zeros in a nd element vector and defines a subset of landmarks which select the points belonging to the two removed bones from the approximation of the full shape vector, $\tilde{\mathbf{x}}$. The parameter η is an additional term introduced to avoid problems of potentially ill-conditioned matrix inversion and over-fitting of the predictors. The matrix Λ contains the retained non-zero eigenvalues of $\mathbf{S}$ (the covariance matrix). This is used to weight the principle components according to their variance. An iterative procedure of solving for the model parameters and estimating the complete shape is continued until convergence of the partial estimate is obtained. This process is outlined as follows:

1. Initialise the mdx1 linear mapping L, set the initial shape parameters to zero and initialise the first mapped partial estimate to $\tilde{\mathbf{y}} = L\tilde{\mathbf{x}}_0$ where $\tilde{\mathbf{x}}_0$ is the mean shape and this mean shape is also taken as the first estimate of the full shape.

2. Align the partial input with first mapped partial estimate using Procrustes.

3. Calculate the new shape parameters $\mathbf{b}_y$ and apply constraints of $\pm 3\sqrt{\lambda_i}$ if necessary.

4. Compute the new estimate of the full shape $\tilde{\mathbf{x}}$ as well as the new mapped partial estimate, $\tilde{\mathbf{y}} = L\tilde{\mathbf{x}}$.

5. Compute the error between old and new mapped partial estimate.

6. Return to step 2 while convergence is not yet established.

3.3 3D object scanner and point digitiser

In order to obtain a partial input with which to estimate the full shape vector (all four bones - third metacarpal, capitate, lunate and scaphoid), points will be digitised off the two removed bones (lunate and scaphoid). Two different methods will be investigated to accomplish this. The first method utilises a mobile-based object scanner which is available on Google's Play Store (Scann3d) and the second utilises a custom-built mobile AR-based application which allows for the digitisation of individual points.

Scann3d captures a series of still images (approximately 20 to 40 sequential images) and uses these images to reconstruct a relatively fine surface mesh which can then be exported as a .stl file (face-vertex data). Downsides to this approach include aspects such as the reliability and accuracy of the mesh generated depending largely on the operator holding the mobile phone as well as on environmental aspects such as lighting or the presence of reflective surfaces. Furthermore, due to these limitations some geometric features may not be captured or appear less prominent to a certain extent. The 3D object scanner does however allow for coverage from almost all view points and the resulting mesh can be used to establish correspondence using the CPD algorithm after which the shape estimation procedure can be carried out.

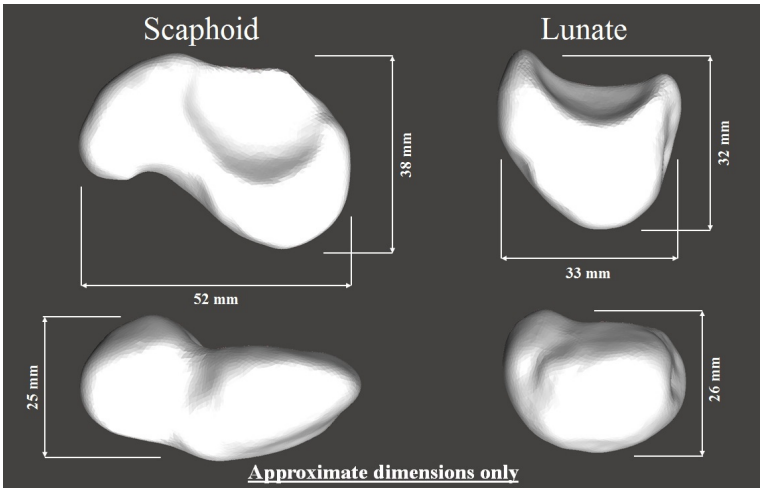

Figure 3.11: Approximate dimensions of 2:1 scale 3D printed scaphoid and lunate.

The accuracy of this approach will be tested using 3D printed models of the lunate and scaphoid from a single subject (scale of 2:1 - approximate dimensions shown in Figure 3.11). A scale of 2:1 was used due to geometric features being captured more easily at a larger scale. Scann3d is then used to create a surface mesh of each of the two physical bones (Figure 3.12). Each mesh is then

refined to a certain extent by removing unwanted or background geometry and then roughly aligned which is a prerequisite for establishing correspondence. Correspondence ensures that each mesh generated from the 3D scanner has the same number of landmarks as the original meshes used for 3D printing. The scanned (post-correspondence) and original meshes are then centered at the origin and aligned using Procrustes Analysis after which they can be compared to one another by looking at the mean absolute error (MAE) of each of the generated meshes. This process can then be repeated using the same two 3D printed bones.

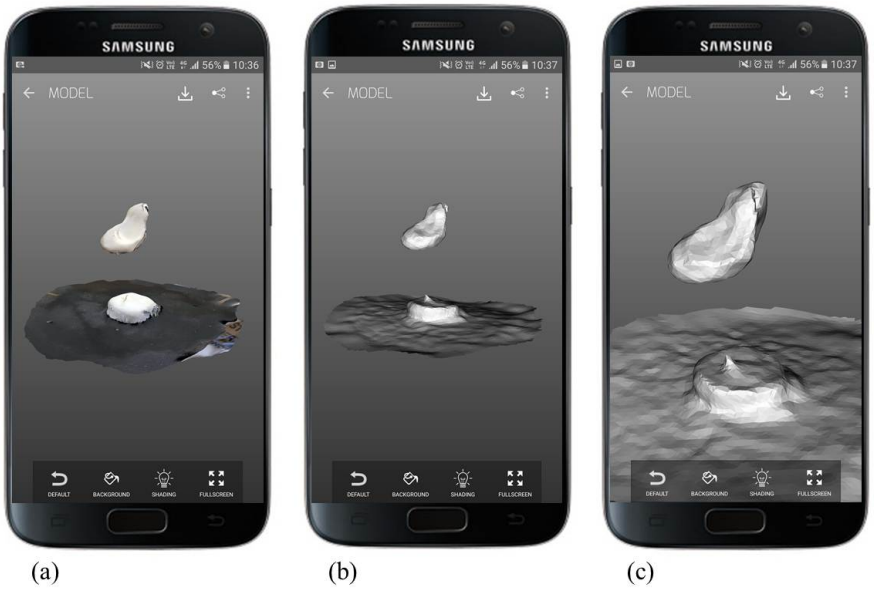

Figure 3.12: Demonstration of Scann3D ("Scann3d | Smartmobilevision") object scanning application using a 3D printed, 2:1 scale scaphoid, (a) screenshot of the reconstructed 3D model with texture, (b) resulting mesh, (c) close-up of resulting mesh.

The second method makes use of a custom-built mobile AR-based application (developed with the Unity Game Engine) which allows for the digitisation of individual points on the surface of each of the two surgically removed bones. This is accomplished by using the phone's camera (and the Vuforia SDK plugin for Unity) to track two separate image markers, one being the reference marker while the other being used to track the position of the point to be digitised (the tip of a stylus-like implement), relative to the reference marker. One advantage of this approach is that it does not require images to be patched together to create the 3D shape of the physical object. Furthermore, it is not sensitive to reflective surfaces as such and specific geometric features or

landmark points can be captured which otherwise might be lost with the first method used (Scann3d). The user can digitise as many anatomical landmarks as desired and also record additional pseudo-landmarks, which is advantageous for performing rough alignment using Procrustes. Once the user is satisfied with the points selected, the positional information of the recorded points can be saved into a .csv (comma-separated values) file and exported for further use.

The accuracy of this application will be tested firstly by capturing several predetermined landmark points on a flat reference image marker. With the dimensions and scale of both image markers (reference marker and the marker placed on the stylus-like implement) fixed, the true positions (in mm) of these points are known (e.g. at the center $[0, 0, 0]$ or at the top right corner $[82.5, 63.5, 0]$) which allows for the calculation of an absolute error with respect to these true positions. To get an idea of scale, the flat reference image marker has dimensions of 165 mm and 127 mm along its length and breadth, respectively. This process can be repeated a number of times (Figure 3.13).

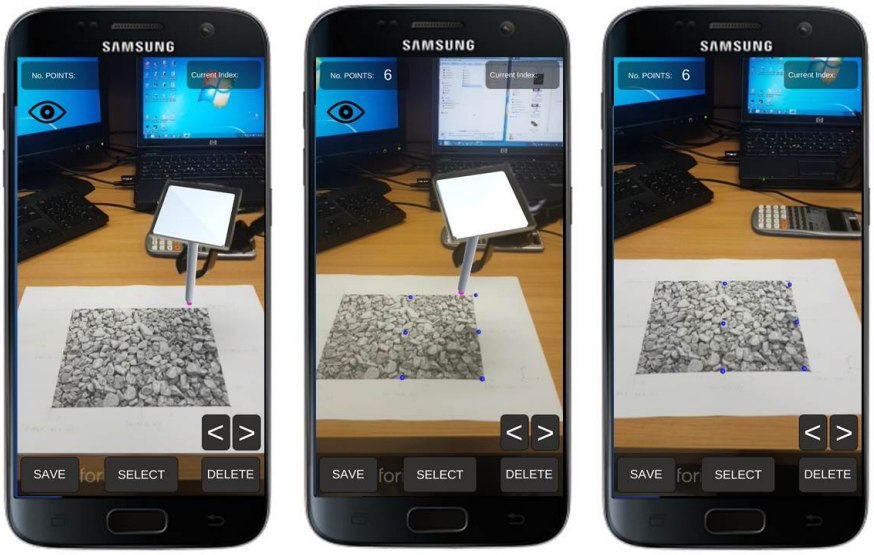

(a) (b) (c)

Figure 3.13: Utilising the digitising application to record points with known positions on a flat image marker.

Next, a simple 3D printed jig with predetermined landmark points will be used to further test the digitising application. Again, with the dimensions and scale of both image markers and the 3D printed ramp fixed, the true positions of 10 predetermined landmark points are known relative to the reference image

marker. To get an idea of the scale of the ramp, the flat reference image marker used here is the same as that used previously with dimensions of 165x127 mm and the dimensions of the ramp are shown in Figure 3.14. The corresponding digitised points can be recorded and compared with their true positions by looking at the MAE (Figure 3.15) between the two.

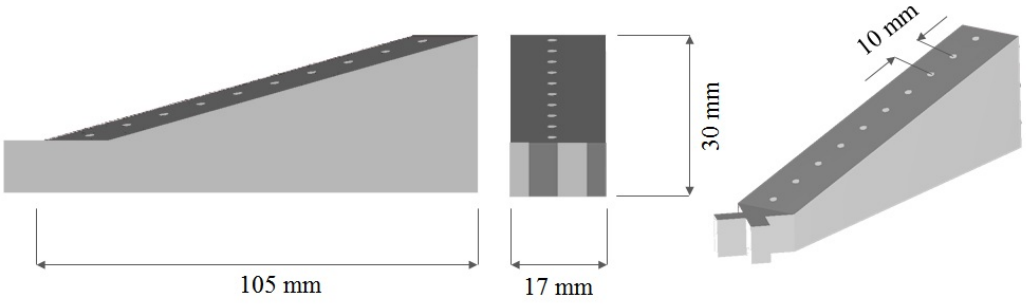

Figure 3.14: Dimensions of 3D printed ramp.

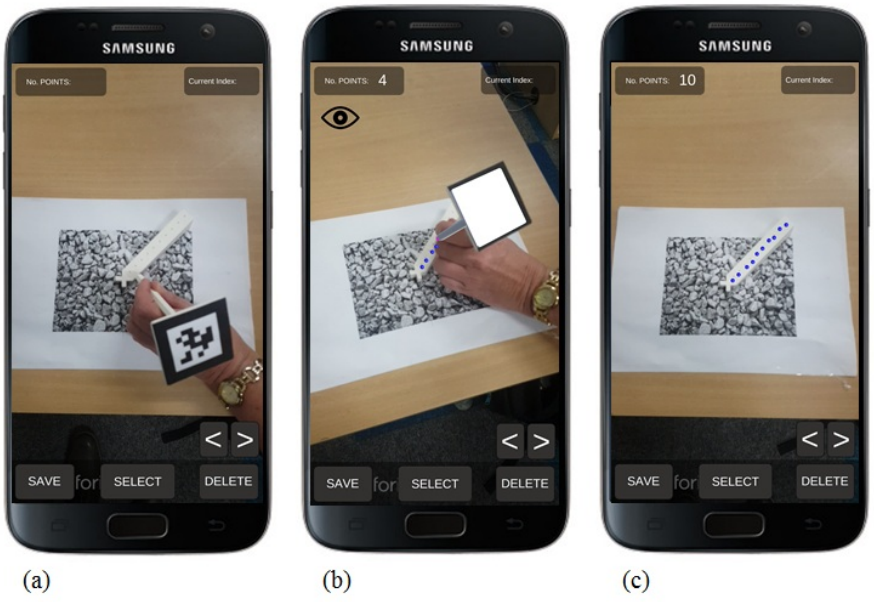

Figure 3.15: Utilising the digitising application to record points with known positions on a 3D printed ramp.

Lastly, the digitising application will then also be tested by digitising points off the same two 3D printed bones utilised in the first method incorporating

the 3D object scanner from Scann3d. Once the selected landmarks have been recorded using the digitiser, these points can then be roughly aligned and used to find correspondences with the original meshes used for 3D printing. Once correspondence has been established, the MAE between the meshes used for 3D printing and that obtained from the digitisation-correspondence process can be calculated (Figure 3.16). This process can be repeated on a number of occasions for each of the two 3D printed bones.

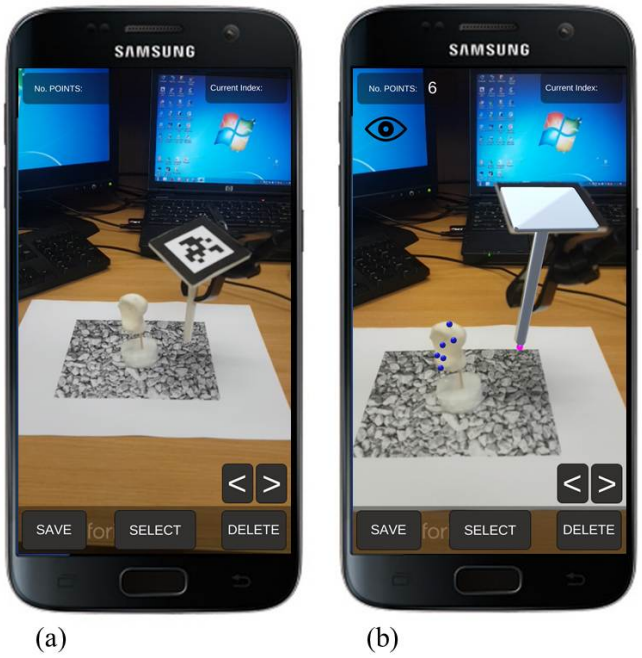

(a) (b)

Figure 3.16: Utilising the digitising application to record points on the surface of a 3D printed 2:1 scale scaphoid.

3.4 Augmented reality concept application and experimental set up

One of the most important navigational aspects of wrist replacement surgery is the process of guide wire insertion. Surgeons rely on guide wires to ensure the correct placement and trajectory of drills, with a drill bit fitting over the guide wire (referred to as a canulated drill). Referring back to Figure 3.3, Figure 3.4 and the associated text in Section 3.1.2 outlining the surgical procedure, it was mentioned that in order to ensure proper orientation of the guide wire (on two occasions - insertion into distal radius and insertion through the capitate-third metacarpal pair), it is important that the surgeon have a true A/P and lateral view of the operating site. The process of guide wire insertion thus involves

acquiring numerous fluoroscopic images which expose both the patient and the surgeon to large amounts of radiation. The importance of correct guide wire placement and drill orientation was also mentioned in Section 3.1.2 together with the associated consequences thereof.

Due to the importance of guide wire insertion and proper drill orientation (which depends largely on the correct placement of the guide wire), it was decided that for an experimental test set up, it would be sufficient to simulate the process of guide wire insertion only. This would be done under conventional image-guided navigation (fluoroscopic) as well as under AR-guidance.

A simple experiment was designed which consists of a section of PVC pipe 100 mm in length and a 50 mm diameter with a 3D printed flange fitted onto one end. The other end would be open and serve as the entry point for the guide wire while the flanged end will be closed incorporating an off-centered circular target which is not visible to the operator. The center of this target will be what the surgeon takes aim for when inserting the guide wire. The cylinder itself will be filled with a rigid foam to simulate the resistance felt when advancing a guide wire through cancellous bone (spongy bone). Drilling along a tube towards an obscured target is therefore a simplified procedural situation in a controlled environment and is not an attempt to replicate the entire procedure outlined in Section 3.1.2.

Positional tracking of the large cylinder (and thus the target to take aim at) is accomplished using a cylindrical image marker wrapped around its circumference. A second, flat image marker is attached to the near end of the guide wire to enable the tracking of the tip at its far end. This experimental set up is shown in Figure 3.17 and Figure 3.20(a-b).

The simulated task will be carried out by an orthopaedic surgeon first under fluoroscopic guidance using a series of 2D images (Figure 3.19) only and then under AR guidance (repeating each experiment a number of times - in this case on 20 occasions). This will allow for a direct comparison to be made with regards to the number of intraoperative fluoroscopic images required (radiation exposure), “operating time”, as well as the accuracy to which the surgeon can reach the center of the target. Accuracy will be measured by recording the radial distance (in mm) from the center of the target (goal impact point) to the actual impact point achieved (Figure 3.18). Furthermore, qualitative results such as ease-of-use or intuitiveness can also be obtained via a post-procedure debriefing. In both cases the surgeon would otherwise be unaware as to the location of the "anatomical target" in the absence of intraoperative navigational guidance.

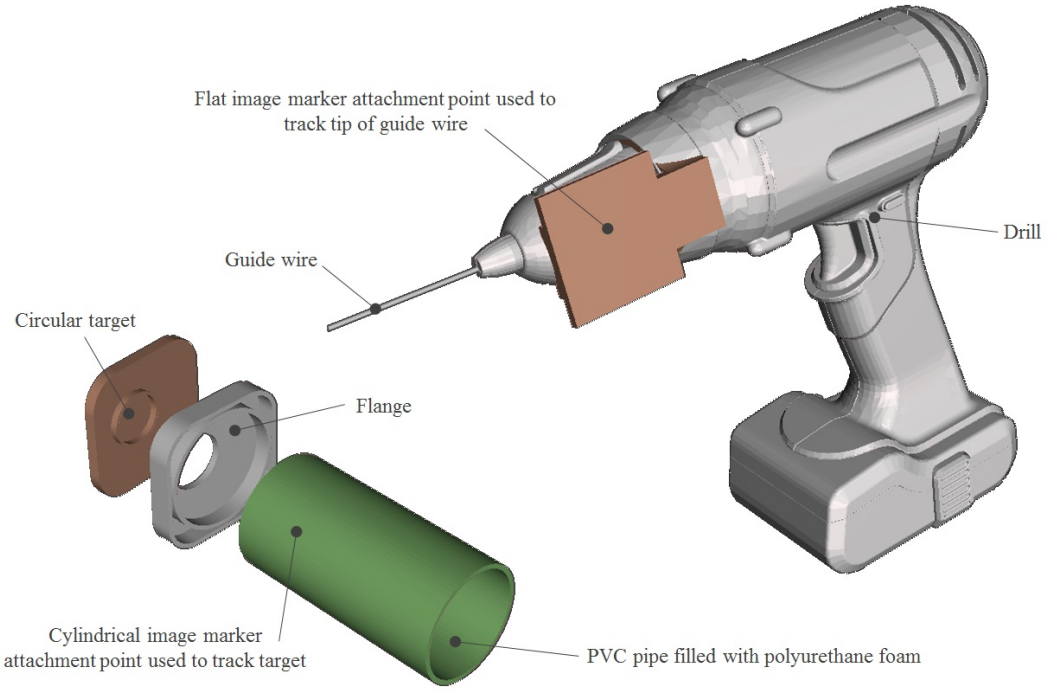

Figure 3.17: Components which comprise the experimental set up

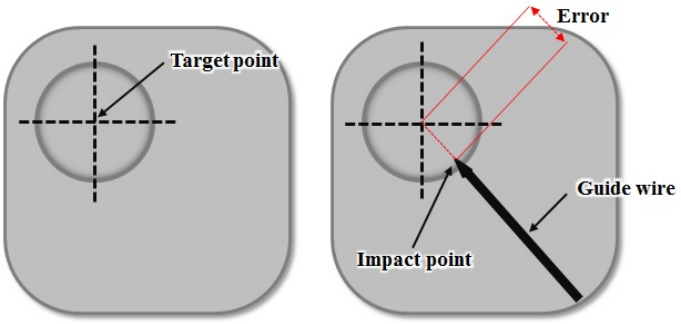

Figure 3.18: Defining the error for a measure of accuracy

Using an AR application with a head-mounted display (HMD) will allow the surgeon to see a digital image of the target in its correct "anatomical" position, the location of the guide wire tip (and distance to the center of the target) as well as the current and ideal trajectory of the guide wire (Figure 3.20(c)) together with an indicator for when these two trajectories are aligned (within a certain tolerance). The ideal trajectory is calculated by determining the gradient of the shortest path between the tip of the guide and the centre of the target with respect to the reference image marker (marker wrapped around cylinder). The current trajectory is simply the gradient of the guide wire with

respect to the reference image marker. On each occasion when carrying out the experiment, the starting or entry point into the foam filled cylinder is chosen arbitrarily.

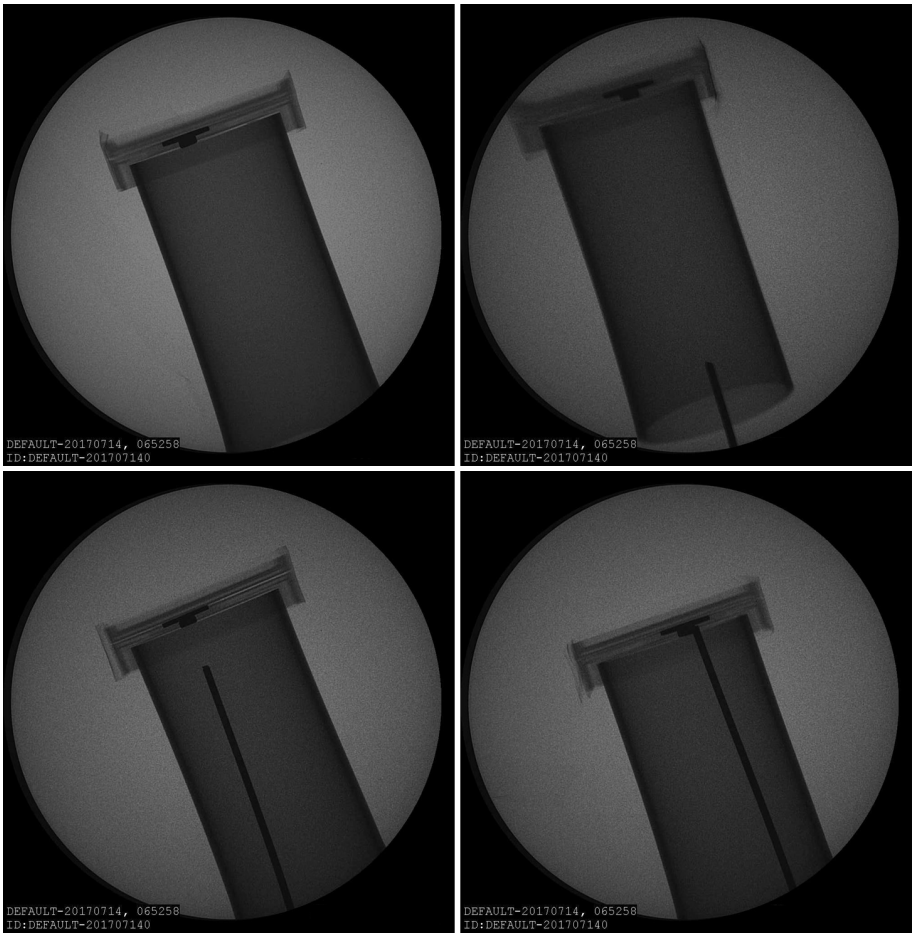

Figure 3.19: Experimental set up under fluoroscopic guidance

In terms of the hardware used with this experiment, a Samsung Galaxy S7 smartphone (shown in Figure 3.13) is used in conjunction with a video see-through (VST) HMD (similar to that shown in Figure 2.8(b)) to provide the surgeon with a heads-up view of the augmented reality scene. The AR environment used to build the application is that of the Unity Game Engine and the tracking of the two image markers was accomplished by making use of Vuforia's SDK plugin for Unity. The advantages of utilising smartphone-based platforms were mentioned in Section 1.3.

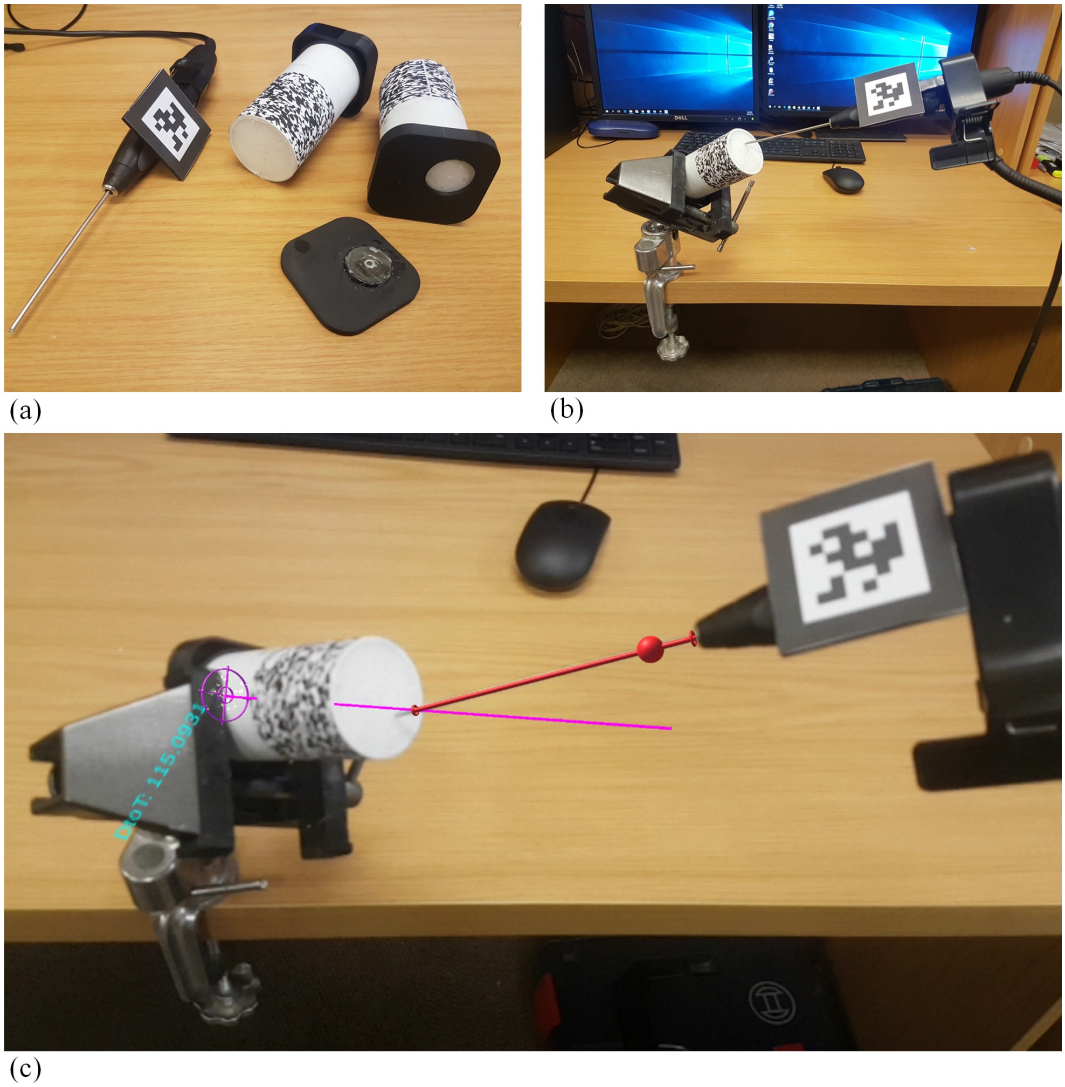

Figure 3.20: Photographs showing the experimental set up and AR navigational assistance (a-b) Experimental set up (c) AR navigational assistance provided

In this study, due to external factors, a VST HMD is used to perform the simulated procedure under AR guidance which unfortunately does not provide the surgeon with any sense of depth when making use of his/her hands. This forces the surgeon to rely entirely on the navigational assistance provided by the augmented content and can be a limiting factor for obvious reasons. If an optical see-through (OST) HMD were to be used, this may enhance the experience and intuitiveness of AR-guided surgery which could have a positive impact on the results observed.

3.5 Summary

This chapter addressed the tools and techniques used to realise the conceptual workflow outlined in Section 3.1.3. Two methods of digitising points off the two removed bones were given and how the output from these two methods would be used as an input into the shape estimation procedure which incorporates a SSM. The steps involved for the integration of the digitisation process into the the shape estimation algorithm were outlined. However, the output (full shape vector) from the shape estimation procedure was not used during the testing of the simulated AR-guided procedure outlined in Section 3.4. This integration is therefore lacking, but the simplicity of the simulated procedure, which is a simplification of one key aspect in the actual procedural workflow for wrist replacement procedures outlined in Section 3.1.2, still allows for the desired results to be obtained. The main outcomes which the AR experiment aims to address can be summarised by the following questions: "Is AR-guidance more or less accurate than more conventional forms of navigational assistance (i.e. fluoroscopic)?", "Can procedural time be reduced with using AR-guidance?", "Can AR-guidance provide a means of reducing or eliminating the need for multiple intraoperative fluoroscopic screenings and therefore reduce radiation exposure for both the patient and surgeon?", "Is AR-guided surgery more or less intuitive than other, more conventional forms of navigational assistance?", and lastly, "Is the technology feasible for widespread use in the OR?". It is believed that the simulated AR-guided procedure designed, although simple, has all the characteristics needed in order to answer these questions.

Chapter 4

Results

This chapter includes the results from the validation of the Statistical Shape Model (SSM) with values for generality, specificity and compactness calculated and graphed as a function of the number of retained modes of variation. Next, results pertaining to the accuracy of the 3D object scanner (Scann3d) as well as the custom-built AR-based point digitising application are given. Following this are the results of using these methods to obtain a partial input with which to estimate the full shape vector of all four bones (third metacarpal, capitate, lunate and scaphoid) by incorporating the SSM. Furthermore, the results from the AR concept application discussed in Section 3.4 are provided. Completing the chapter are discussions on the various sets of results gathered.

4.1 Validation of statistical shape model

The number of landmarks utilised in the construction of the SSM were 30504, 12540, 11532 and 7938, for the third metacarpal, capitate, scaphoid and lunate respectively, or 62514 landmarks in total. No significance was placed on size of each mesh, however, a sufficient number of landmarks were ensured such as to obtain good correspondence (i.e. as a rule of thumb utilising more landmarks results in improved correspondence, to a certain extent).

Figure 4.1(a-d) shows the results from the validation of the SSM for the first 48 modes of variation. Figure 4.1(a) shows the percentage variance for each mode. It can be seen that the first mode accounts for 12.27 % of the variance with the second and third modes accounting for 10.07 % and 7.58 % of the variance respectively. $K_{98\%}$ (model represents 98 % of the total variance of the data) was reached at mode 48. Figure 4.1(b) is a plot of the accumulative variance in the shape data. Generality (Figure 4.1(c)) ranged between 0.026 and 0.034 mm for the third metacarpal, 0.057 and 0.075 mm for the capitate, 0.059 and 0.075 mm for the scaphoid and 0.059 and 0.074 mm for the lunate. Values for specificity (Figure 4.1(d)) ranged between 0.04 and 0.11 mm for the

third metacarpal, 0.10 and 0.26 mm for the capitate, 0.15 and 0.28 mm for the scaphoid and 0.11 and 0.27 mm for the lunate. It is important to note that the values indicated are unscaled, however, of more interest is that of the overall trends in generality, specificity and compactness.

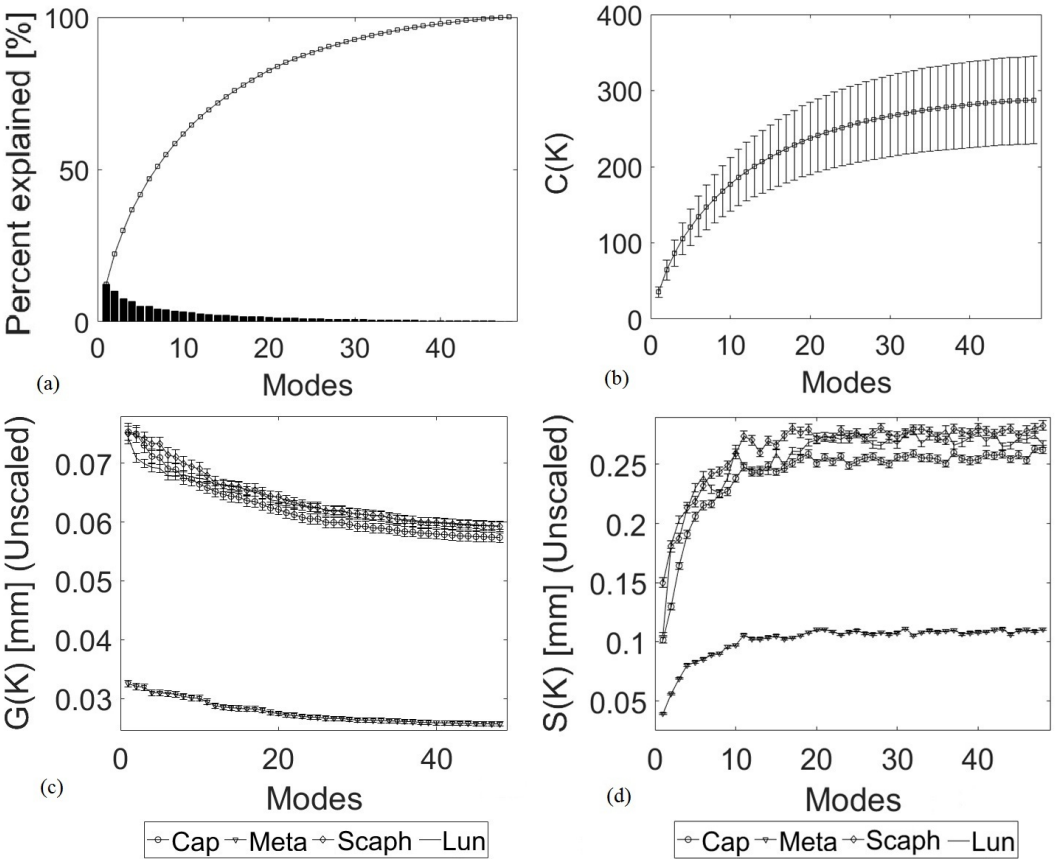

Figure 4.1: Values for generality, specificity and compactness for the first 48 modes of variation. Pareto diagram also given.

4.2 Accuracy of 3D object scanner and point digitiser

The results of utilising the custom-built AR-based point digitising application on a flat reference image marker (as shown in Figure 3.13 in Section 3.3) with 6 predetermined landmark points of interest (true positions known) are shown in Table 4.1. The mean absolute error (MAE) between the recorded positions and the true positions of each landmark point was calculated. This process was repeated on 5 occasions. The results indicate an average MAE of 3.63±1.49 mm for all points recorded and on all attempts. Next, the same application was used on a simple diagonally-inclined 3D printed ramp (as shown in Figure

3.14 and 3.15 in Section 3.3). The MAE between each of the 10 digitised points and their true positions was calculated. This process was repeated on 20 occasions. These results are summarised in Table 4.2. The MAE for all points recorded and on all attempts averaged at 3.64±1.45 mm.

Table 4.1: Results of utilising the point digitising application to record points on a flat image marker.

	Reference Coordinates [mm]			Absolute Error [mm]					Mean Absolute Error (per point) [mm]
	x	y	z	Attempt 1	Attempt 2	Attempt 3	Attempt 4	Attempt 5	
Point 1	0.00	0.00	0.00	3.62	1.55	2.22	2.93	3.65	2.79±0.91
Point 2	0.00	0.00	63.50	3.64	3.59	2.07	3.89	4.81	3.60±0.99
Point 3	82.50	0.00	63.50	4.84	3.29	3.89	3.93	5.39	4.27±0.84
Point 4	82.50	0.00	0.00	4.61	2.82	5.34	3.99	1.53	3.66±1.51
Point 5	82.50	0.00	-63.50	7.89	2.85	3.24	6.89	2.87	4.75±2.44
Point 6	0.00	0.00	-63.50	2.48	1.41	3.65	1.97	4.17	2.73±1.15
Mean Absolute Error (per set of 6 points) [mm]				4.51±1.86	2.58±0.90	3.40±1.20	3.93±1.65	3.74±1.39	

Mean Absolute Error of all points recorded: 3.63±1.49 mm

Table 4.2: Results of utilising the point digitising application to record points on a 3D printed ramp.

	Reference Coordinates [mm]			Absolute Error [mm]							Mean Absolute Error (per point) [mm]
	x	y	z	Attempt 1	Attempt 2	Attempt 3	Attempt 4	Attempt 5	...	Attempt 20	
Point 1	6.46	11.20	8.11	1.76	2.96	2.84	4.72	5.80	...	3.99	3.43±1.30
Point 2	13.54	13.20	15.18	4.39	3.99	5.32	3.88	4.83	...	4.43	3.62±1.29
Point 3	20.61	15.20	22.25	3.51	2.89	3.03	4.53	3.82	...	3.93	3.51±1.27
Point 4	27.68	17.20	29.32	4.15	2.28	3.27	5.17	3.96	...	3.75	3.25±1.12
Point 5	34.75	19.20	36.39	3.97	3.79	5.25	4.15	4.39	...	3.00	3.58±0.99
Point 6	41.82	21.20	43.46	3.64	6.84	3.04	4.45	4.10	...	3.36	4.22±1.66
Point 7	48.89	23.20	50.53	4.15	4.24	5.34	4.76	4.37	...	3.26	3.93±1.33
Point 8	55.96	25.20	57.60	5.16	5.85	4.82	4.14	5.28	...	3.68	4.35±1.29
Point 9	63.03	27.20	64.68	4.91	6.30	7.03	5.75	4.63	...	4.25	4.50±1.79
Point 10	70.10	29.20	71.75	3.52	6.08	5.38	4.18	5.02	...	2.80	4.53±1.94
Mean Absolute Error (per set of 10 points) [mm]				3.91±0.94	4.52±1.63	4.53±1.41	4.57±0.56	4.62±0.62	...	3.64±0.53	

Mean Absolute Error of all points recorded: 3.64±1.45 mm

The results of utilising the 3D object scanner from Scann3d to obtain meshes for both the 3D printed scaphoid and lunate (as shown in Figure 3.12 in Section 3.3) are presented in the first row of Table 4.3. The best results achieved with the 3D object scanner had a post-correspondence MAE of 1.43±0.63 mm and

1.78±0.67 mm for the lunate and scaphoid respectively. On average, the results indicate a MAE of 2.53±1.05 mm for the lunate and 3.04±1.37 mm for the scaphoid. The results obtained were at a scale of 2:1 (twice the true anatomical size, but the same size as the 3D printed models).

Table 4.3: Accuracy of 3D object scanner and point digitising application tested on a 2:1 scaled 3D printed scaphoid and lunate.

		Mean Absolute Error and Deviation [mm]					Averaged over 5 attempts [mm]
		Attempt 1	Attempt 2	Attempt 3	Attempt 4	Attempt 5	
3D Object Scanner (Scann3d)	Scaphoid	2.49±0.98	3.88±1.47	1.43±0.63	3.04±1.20	1.82±0.75	2.53±1.05
	Lunate	3.73±1.82	1.78±0.67	3.65±1.46	2.87±1.42	3.17±1.21	3.04±1.37
Point Digitiser (5 points)	Scaphoid	1.95±0.54	1.54±0.40	1.24±0.39	1.76±0.72	1.50±0.48	1.60±0.52
	Lunate	2.33±0.77	1.67±0.68	1.65±0.40	1.94±0.75	1.77±0.48	1.87±0.63
Point Digitiser (20 points)	Scaphoid	4.42±1.75	3.83±1.81	5.12±2.42	6.57±2.30	6.24±2.21	5.24±2.12
	Lunate	7.69±2.71	6.75±3.63	4.88±2.39	5.72±2.51	7.44±2.52	6.50±2.79

The results of utilising the AR-based digitising application to digitise points on the surfaces of both the 3D printed scaphoid and lunate (as shown in Figure 3.16 in Section 3.3) are presented in the second and third row of Table 4.3. On the first occasion only 5 landmark points were used, thereafter a further 15 random pseudo-landmark points were added. The post-correspondence MAE was calculated for each individual point in the mesh and then averaged over all points. This process was repeated on 5 occasions for both the scaphoid and lunate. On average, the results indicate a MAE of 1.60±0.52 mm for the lunate and 1.87±0.63 mm for the scaphoid when only the 5 initial landmark points are used. For the case when 20 points were used, MAE results of 5.24±2.12 mm and 6.50±2.79 mm were obtained for the lunate and scaphoid, respectively. Again, these results were obtained at a scale of 2:1.

4.3 Shape estimation

Figure 4.2 shows the relationship between the reduction in points used to establish correspondence (i.e. the points obtained from the 3D object scanner or point digitiser) and the average unscaled error for the resulting output from the shape estimation process. This was carried out on each of the 50 training shapes, hence error bars are used to indicate the mean and deviation in mean, both in terms of the error and in the number of vertices which make up each pre-correspondence shape. Figure 4.2(a) makes use of a partial input obtained from the lunate only and Figure 4.2(b) is that of using the scaphoid only. Figure 4.2(c) is the result obtained when both bones are used as a partial input.

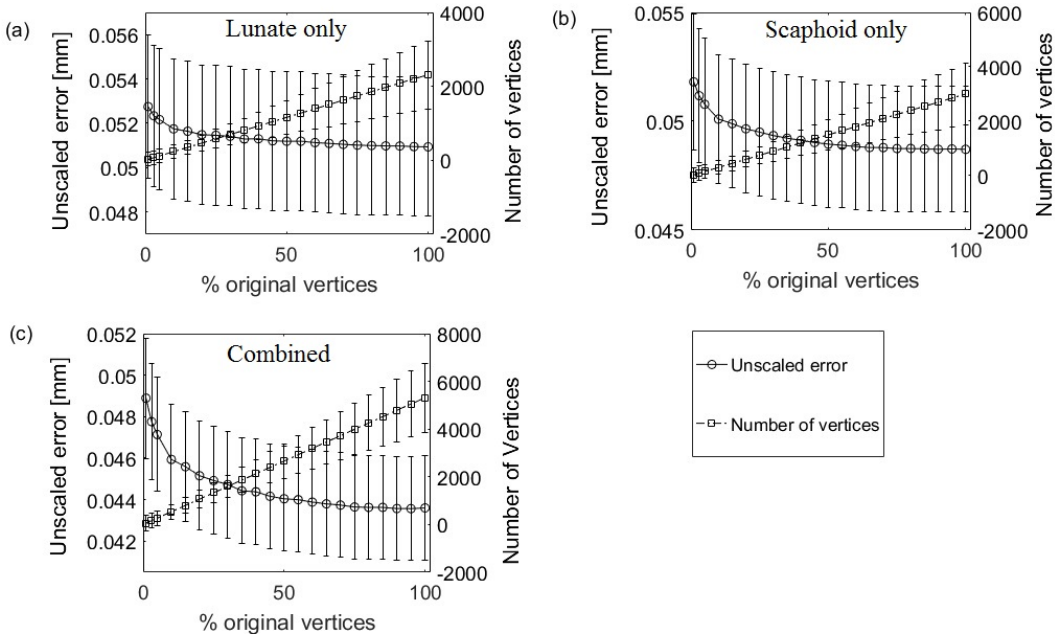

Figure 4.2: Relationship between the accuracy in the estimate of the full shape vector versus the number of points used to establish correspondence with the two removed bones.

Table 4.4: Accuracy of the shape estimation output when making use either the 3D object scanner or the point digitising application.

		Mean Absolute Error and Deviation (Unscaled) [mm]					Averaged over 5 attempts [mm]
		Attempt 1	Attempt 2	Attempt 3	Attempt 4	Attempt 5	
Partial input obtained by utilising 3D object scanner	**Scaphoid only**	0.102±0.061	0.102±0.061	0.102±0.061	0.102±0.061	0.102±0.061	0.102±0.061
	Lunate only	0.076±0.051	0.050±0.030	0.089±0.056	0.083±0.051	0.081±0.051	0.076±0.050
	Scaphoid and Lunate	0.091±0.058	0.072±0.047	0.098±0.061	0.092±0.056	0.081±0.051	0.087±0.055
Partial input obtained by utilising point digitiser	**Scaphoid only**	0.050±0.035	0.049±0.032	0.051±0.035	0.051±0.036	0.052±0.039	0.051±0.036
	Lunate only	0.069±0.042	0.072±0.045	0.067±0.042	0.063±0.039	0.074±0.045	0.069±0.043
	Scaphoid and Lunate	0.071±0.045	0.073±0.047	0.069±0.045	0.067±0.042	0.079±0.050	0.072±0.046

The results of utilising both the 3D object scanner and the point digitising application to obtain a partial input with which to estimate the full shape (third metacarpal, capitate, lunate and scaphoid collectively) are shown in Table 4.4. Three different partial inputs were explored. The first being that when only the lunate is used as a partial input, the second being when only the scaphoid is used and the last case makes use of both the scaphoid and lunate as the partial input. Best results were obtained when making use of a partial input consisting of the lunate only and by making use of the point digitising application (recording 5 landmark points) with an unscaled MAE of

0.051±0.036 mm. Correctly scaling the error values for each of the four bones according to their true anatomical size indicate a MAE of 1.72±0.80 mm for the third metacarpal, 1.83±0.86 mm for the capitate, 1.63±0.64 mm for the scaphoid and 1.69±0.76 mm for the lunate.

4.4 AR concept application and simulated procedure

The simulated experiment was carried out on 20 occasions under either fluoroscopic guidance or AR guidance only (as outline in Section 3.4). These results are presented in Table 4.5. A radial tolerance of 1.5 mm was placed on the alignment indicator between the ideal and actual trajectories.

Table 4.5: Results of conducting the simulated procedure under fluoroscopic and AR assistance noting the time-to-completion, accuracy and number of screenings.

	Fluoroscopic Assistance			AR Assistance		
	Time [s]	Accuracy [mm]	No. of screenings	Time [s]	Accuracy [mm]	No. of screenings
Attempt 1	45.14	6.64	6	16.73	6.38	-
Attempt 2	42.63	5.51	5	19.18	7.07	-
Attempt 3	47.67	23.91	8	18.43	20.93	-
Attempt 4	35.56	16.50	6	26.19	24.10	-
Attempt 5	55.31	13.89	9	27.98	2.66	-
Attempt 6	38.51	4.25	7	25.28	6.40	-
Attempt 7	32.98	7.20	5	28.24	2.26	-
Attempt 8	41.21	7.87	7	22.58	3.31	-
Attempt 9	31.16	5.21	5	15.82	1.51	-
Attempt 10	44.74	7.94	5	21.72	10.14	-
Attempt 11	34.07	3.51	4	19.73	18.15	-
Attempt 12	38.90	2.16	5	26.62	2.57	-
Attempt 13	37.58	10.71	5	35.82	19.08	-
Attempt 14	28.98	7.02	4	22.48	2.57	-
Attempt 15	34.26	18.42	6	19.99	8.99	-
Attempt 16	31.08	7.03	7	21.59	8.85	-
Attempt 17	36.76	7.78	4	19.46	17.28	-
Attempt 18	40.45	9.58	5	21.45	3.38	-
Attempt 19	37.05	6.78	5	19.71	16.62	-
Attempt 20	33.45	8.59	5	18.77	2.11	-
Mean and deviation (Excl. outliers)	37,17±4,77	6,74±2,13	5,00±0,97	21,68±3,57	8,70±7,00	-

A box-and-whisker diagram was constructed for both time-to-completion and accuracy recordings to identify outliers (Figure 4.3(a-b)). The most noticeable features of these plots are that of the large interquartile range observed in the

accuracy under AR guidance as well as a large number of "outliers" in the accuracy measurements under fluoroscopic guidance. Excluding these outliers (indicated by the dark grey filled rows in Table 4.5), a plot of accuracy (error) versus time for all attempts under fluoroscopic and AR guidance is given in Figure 4.4.

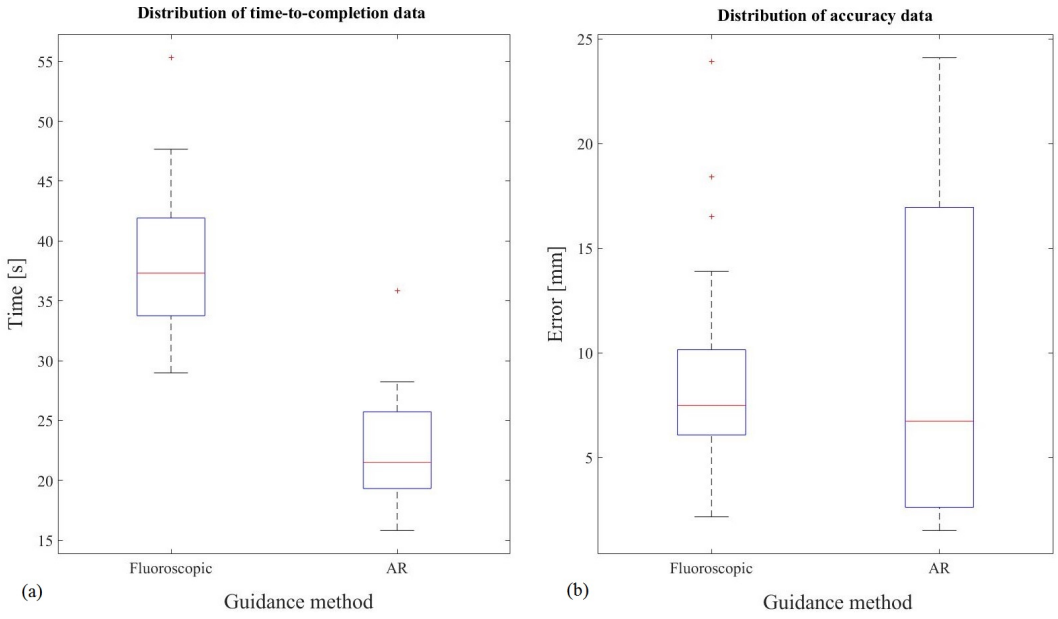

Figure 4.3: Box-and-whisker plot constructed for both time-to-completion and accuracy recordings. Outliers indicated.

On average (excluding outliers), the time it took to complete the simulated procedure under fluoroscopic assistance was 37.17±4.77 s and 21.68±3.57 s in the case of AR assistance being used. In terms of accuracy, a mean value of 6.74±2.13 mm and 8.70±7.00 mm was achieved under fluoroscopic and AR assistance, respectively. The average number of fluoroscopic screenings taken was 5.00±0.97 resulting in an mean radiation exposure level of 0.02 mGy (0.004 mGy/exposure). An F-test is used to compare the variation of the two sample sets with p value of 0.23 being obtained for time-to-completion and a value of $<<0.01$ for accuracy (values rounded to two significant figures). A p value less than 0.05 indicates that the variance of the two sample sets are significantly different (statistically significant). Moreover, to compare the means of the two sample sets, a T-test (based on the values obtained from the F-tests) is used. The results from the T-test indicate a p value of $<<0.01$ and 0.27 for time-to-completion and accuracy, respectively. Again a p value less than 0.05 indicates a significant difference in the means.

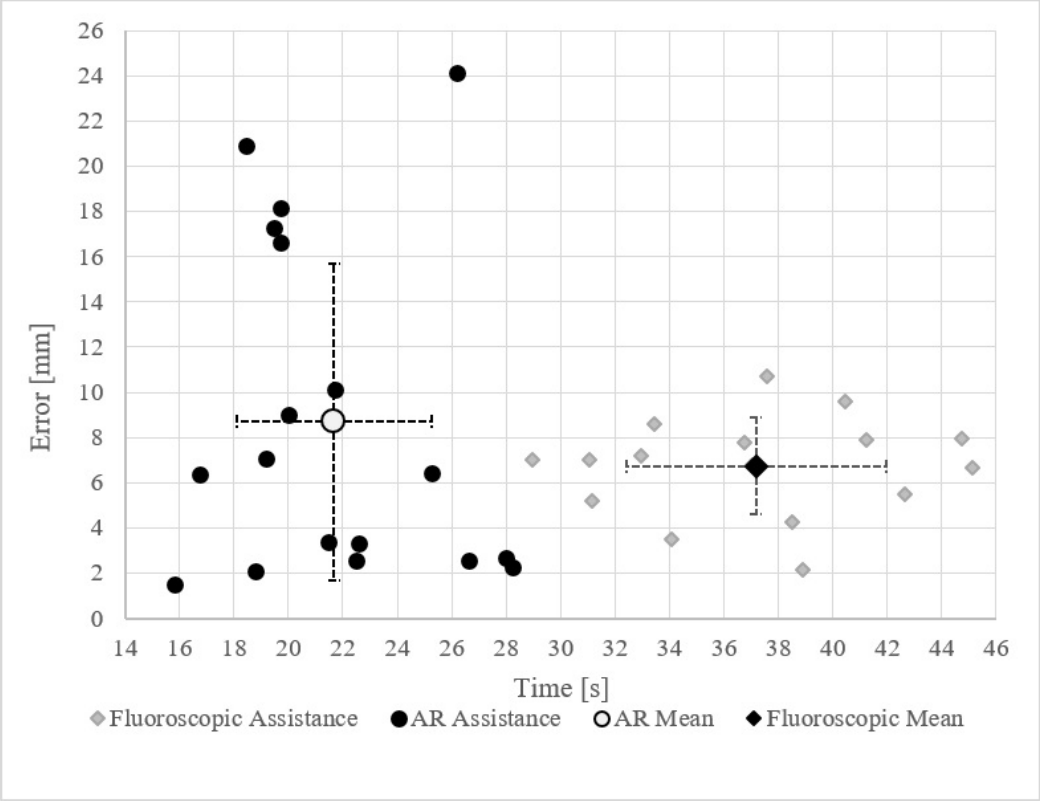

Figure 4.4: Plot of accuracy versus time for the simulated procedure under fluoroscopic and AR guidance.

4.5 Discussion of results

In this section, a discussion of each set of results is provided. Furthermore, an attempt is made to relate the results gathered here as best as possible, to that found in existing literature. However, due to the difficulty in finding past studies encompassing work across all the subsections covered in this study, each section has been discussed independently from the other such to allow for reasonable comparisons to be made and conclusions to be drawn.

4.5.1 Statistical Shape Model

In terms of Section 4.1 covering the validation of the SSM, predominantly of interest is that of the overall trends in generality, specificity and compactness with lower values indicating an improvement in each measure respectively. With $K_{98\%}$ being reached at mode 48 this implies that 98 % of all variation is explained by the SSM at that point. The values obtained for generality and specificity are unscaled. This is due to a single shape model being used to model the variation within the group of bones as a whole (third metacarpal,

capitate, lunate and scaphoid) rather than four separate shape models for each of the bones in question. With a SSM one would ideally want to eliminate any variation due to pose and scale, hence reintroducing scale into the validation results is somewhat problematic and in this case was thought to be unnecessary.

Another issue with modelling all four bones collectively in a single SSM is that information pertaining to relative pose and scale between the group of four bones is lost. Each of the four bones was scaled to unity and centered at the origin and as such the output from the shape model is also a set of four bones, all centered at the origin and each scaled to unity. This was done to avoid potential problems when establishing correspondence and to avoid physically impossible multi-object pose scenarios (overlapping of joints).

One possible solution which could solve this problem is to create a separate, relatively sparse SSM consisting of a small number of landmark points on each of the four bones containing information relating to relative pose and scale. Using the output of the first shape model (purely variation in the shape of each of the four bones) as an input into the second shape model (modelling variation in relative scale and pose), it may be possible to get an output which approximates the correct anatomical layout of the group of bones within the wrist of a particular individual. This approach was not implemented here but if attempted it may be necessary to have a means of selecting reliable anatomical landmarks consistently which already proved to be problematic due to the bones in question being somewhat irregular in shape and with there seemingly being a lack of available morphological studies with suitable information which could assist with landmark selection.

A study by Sebastian *et al.* (2006) addresses the segmentation of carpal bones from CT images using skeletally coupled deformable models. Here they mention that the non-uniformity of bone tissue (ranging from dense cortical bone to textured spongy bone), the irregular shaped and small carpal bones which move with respect to one another and with respect to the CT resolution, the presence of blood vessels and the inherent blurring of CT images renders the segmentation of carpal bones a challenging task. In this work by Sebastian *et al.* (2006) the performance of statistical classification, deformable models (active contours), region growing, region competition, and morphological operations for the automatic segmentation of carpal bones is reviewed. A model which incorporates several of these approaches in a unified framework is then proposed which combines the advantages of active contour models, region growing, and both local and global region competition methods.

With regards to multi-object SSMs, Bindernagel *et al.* (2012) addresses the problem of applying SSMs to the anatomy of joints and their involved bones taking into consideration the variation of joint posture. In this work it is

mentioned that a common idea is not to consider joints at all but to rather employ multiple independent models of the individual bones, however, there are two major shortcomings with taking this approach. Firstly, an objects pose is independent of its adjacent object(s). This allows for arbitrary object poses to result which are not consistent with natural joint postures (e.g indicated in Figure 4.5(a)). Secondly, a SSM might produce an output which causes an overlapping of adjacent objects (e.g. indicated in Figure 4.5(b)) even though it is known that this is physically impossible.

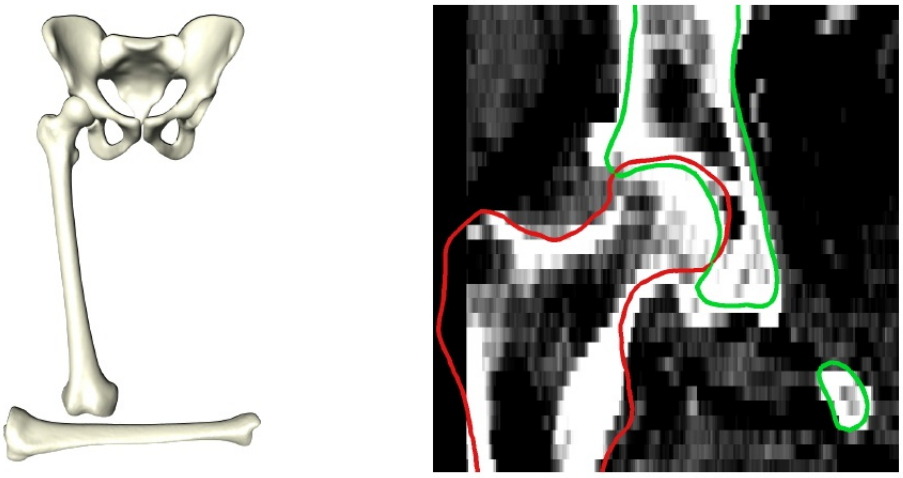

Figure 4.5: Shortcomings of individual SSMs representing a compound of objects. (a) The human lower limb in an anatomically very unnatural state as it may be represented by individual SSMs of pelvis, femur and tibia, (b) Failed hip segmentation by individual SSMs of pelvis (green) and femur (red): The shapes of the acetabulum of the pelvis and the femoral head do not match and thus produce an overlapping segmentation (Image: Bindernagel, n.d.; Kainmuller *et al.*, 2009).

A study by Kainmuller *et al.* (2009) made use of an articulated SSM (ASSM) of the human hip in an effort to increase the reconstruction accuracy of a fully automated CT image segmentation scheme of the pelvis and femur. Similarly, inspired by this work, Bindernagel *et al.* (2012) in an attempt to eliminate the previously mentioned shortcomings, integrated multiple standalone SSMs into one model which considers degrees of freedom (DOF) with mutli-object situations. This work presents a generalisation of the ASSM approach to arbitrary articulated structures comprising multiple objects and/or joints and the resulting framework relies upon explicitly modelled joint representations which map anatomical DOF of joint motion onto relative, rigid transformations between adjacent objects. The result of this approach is that anatomically valid states are always ensured. It is thought that a similar approach could

be used here to regain information pertaining to the relative pose and scale of the four bones used in this study (third metacarpal, capitate, scaphoid and lunate), focusing predominantly on the rigid transformations between objects rather than the DOF of joint motion.

4.5.2 3D object scanner and point digitiser

The results of utilising the AR-based point digitising application were presented in Table 4.1 and Table 4.2 for the flat image marker as well as the 3D printed ramp respectively. In both cases, similar results were obtained with the values for the MAE found to be somewhat large considering the scale of the objects being digitised. There are a number of possible sources of error which could contribute to the magnitude of the MAE values obtained. The first being the fact that the digitisation process utilises a stylus-like implement and was carried out manually hence this method is inherently non-exact. The image marker placed on the 3D printed stylus-like implement (used to track its tip) is done so by hand, further contributing to error. Moreover, 3D printing sharp objects or objects with discontinuities can be problematic and may result in less than perfect geometry being present in the 3D print.

All CAD models of the 3D printed parts were imported directly into a Unity project (AR environment) and used with fixed-size image markers in order to avoid scaling issues when placed into the augmented scene and this would allow for distance-based error metrics to be calculated at real-life scaling. Even though this approach was used in an attempt to avoid obtaining potentially ill-scaled measurements, there does however seem to be possible scaling errors present in the application. Although not confirmed, the potential for scaling errors warrants further investigation. If verified to be contributing to error, it may be necessary to compensate for this by incorporating some sort of calibration procedure and to integrate this into the design of the application within Unity itself. Lastly, there may be errors inherent in the image tracking process and this is unfortunately something that will require further investigation and additional expertise. The AR-based digitising application does however seem to produce results that are reasonably consistent and with some improvement may prove to be a viable and accurate method of digitising points on 3D objects.

The results of utilising the point digitiser to record the position of landmark points on the surface of each of the two 2:1 scale 3D printed bones (scaphoid and lunate) and then using these points to establish correspondence in order to produce a dense mesh were given in rows two and three of Table 4.3. Better results were achieved when only 5 landmark points were used compared to using 20 which is in contrast to what is seen in Figure 4.2 in Section 4.3. It is thought that this is because inaccuracies or errors introduced in the digiti-

sation process are compounded as more pseudo-landmark points are recorded therefore resulting in a somewhat distorted post-correspondence mesh being obtained (i.e. pseudo-landmarks do not correspond well).

The results of utilising the 3D object scanner from Scann3d to obtain a relatively fine surface mesh and then using this mesh to establish correspondence with the original meshes used for 3D printing were presented in the first row of Table 4.3. The results achieved with this approach proved to be less accurate than that of using the point digitiser to digitise 5 landmark points, but better than the case of using 20 digitised points. This may be because although the 3D object scanner produces a relatively fine surface mesh with significant details compared to that of the point digitiser, the resulting mesh is somewhat distorted from its true shape due to certain geometric features being suppressed or made to appear less prominent than in reality. This means that the post-correspondence mesh does not accurately represent the true shape of each bone thus resulting in a larger MAE being observed.

Other available digitising systems include products such as the Immersion MicroScribe G2 desktop 3D measuring and digitisation system and the FASTRAK by Polhemus. The MicroScribe G2 is a precision portable digitising arm with a hand-held probe based around optical angle encoders at each of the five arm joints (Figure 4.6(a)). Angular information from the arm is relayed to the host computer through a universal serial (USB) port and allows for the coordinates of points to be determined. Depending on the specific model of MicroScribe used, it is reported that accuracy values ranging from 0.23 to 0.43 mm can be achieved (3d-microscribe, 2017). The FASTRAK is an electromagnetic motion tracking and point digitisation system (Figure 4.6(b)). With this device, an accuracy of 0.76 mm can be achieved with a resolution of 0.005 mm (Polhemus, 2017).

Figure 4.6: Alternative point digitising systems. (a) MicroScribe G2 (Image: GoMeasure3D, 2017), (b) Polhemus FASTRAK (Image: Polhemus, 2017).

No corresponding literature was found with respect to the reconstruction accuracy of object scanners such as that of Scann3d which create a 3D model from a series of 2D images. An alternative technology in the form of 3D laser scanners can also be used to generate 3D models of physical objects. Numerous products in this category exist. Some examples of such devices include the Matter & form MFS1V1 (Figure 4.7(a)) (scan accuracy: 0.43 mm) (Matterandform.net, 2017), Cubify Sense 3D scanner (Figure 4.7(b)) (scan accuracy: 1.0 mm) (Prod.cubify.com, 2017), XYZPrinting Da Vinci 1.0 AiO 3D Printer + Scanner (scan accuracy: 0.25 mm) (Eu.xyzprinting.com, 2017), MakerBot Digitizer (MakerBot, 2017) and the BQ Ciclop 3D Scanner (scan accuracy: 0.5 mm) (CAD House, 2017), amongst others. It is worth mentioning that the resolution of CT images is typically in a range similar to that of the accuracy achievable with these 3D laser scanners (UTCT - University of Texas, 2017). Unfortunately, no literature could be found with respect to AR-based point digitisation applications.

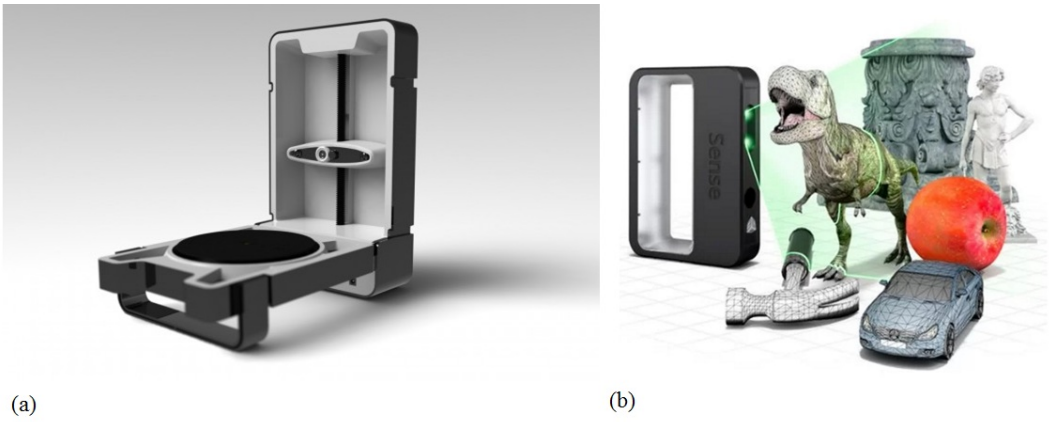

Figure 4.7: Examples of 3D scanners (a) Matter & form MFS1V1 (Image: 3D FilaPrint, 2017), (b) Cubify Sense 3D scanner (Image: toptenreviews, 2017).

4.5.3 Shape estimation

Figure 4.2 in Section 4.3 showed the relationship between the reduction in points used to establish correspondence (i.e. the points obtained from the 3D object scanner or point digitiser) and the average unscaled error for the resulting output from the shape estimation process. It can be seen from all three plots, the average error decreases as the number of digitised points increases (or as mesh density increases). It is believed that this is due to better correspondence being established. It can also be seen from these figures that the error is lowest when both bones are combined to form the partial input to the shape estimation process.

Practically, the shape estimation capabilities of the SSM were tested using the partial inputs obtained from the 3D object scanner and that from the point digitiser (using only 5 landmark points). On average, better results were achieved when using the point digitiser for all three cases of partial inputs (lunate only, scaphoid only and lunate-scaphoid combined input) when compared to those obtained with the 3D object scanner. The best results were achieved when making use of a lunate-only partial input with the point digitiser (5 landmark points). This seems to agree with the results presented in Table 4.3 in Section 4.2 whereby the most accurate post-correspondence mesh was obtained when utilising the point digitiser with 5 landmark points and for the lunate in particular. However, the results do not agree with the trend shown in Figure 4.2 of Section 4.3 whereby better results were achieved when combining partial inputs from both the scaphoid and the lunate. It is thought this is because in a practical sense, errors introduced in the digitisation/3D scanning process for each bone are compounded when both are used as a partial input thus resulting in the larger error observed in the shape estimation process. Scaling the MAE values for the best case scenario (lunate-point digitiser combination), the resulting scaled MAE values lie approximately in the 1-2.5 mm ballpark for all four bones (third metacarpal, capitate, lunate and scaphoid). Error values in this range may be deemed sufficiently accurate for many medical applications (Livyatan *et al.*, 2003), however, improvement in the point digitisation process will likely minimise this error further.

A study by Rajmani *et al.* (2007) looked at statistical deformable bone models for robust 3D surface extrapolation from sparse data. Here, in a similar manner to what was outlined in Section 3.1.3 (refer also to Figure 3.5), a sparse set of landmark points are intraoperatively digitised off the surface of the femur and this sparse and partial input is used to estimate the full shape of the proximal femur. A series of leave-one-out experiments were carried out to evaluate the method. The reconstruction errors of 10 different femurs were calculated first based on 10 digitised points, after which 90 digitised points were used. Surface points were chosen uniformly from the surface model of the left out object and point correspondence was established by finding the closest point. In these experiments the predicted models mean surface error ranged from 0.96 to 2.59 mm with 10 digitised surface points, and the error range decreased to 0.88 to 2.59 mm when 90 digitised points were used. This result is in agreement to the results achieved with a similar process outlined in Sections 3.1.3, 3.2.7 and 3.3 (results given in Section 4.3). A plot of the reconstruction error versus the number of points is shown (Figure 4.8(a)). The trend seen in this plot is similar to that seen in Figure 4.2(a-c). It was observed in two cases that the error actually increased with more surface points.

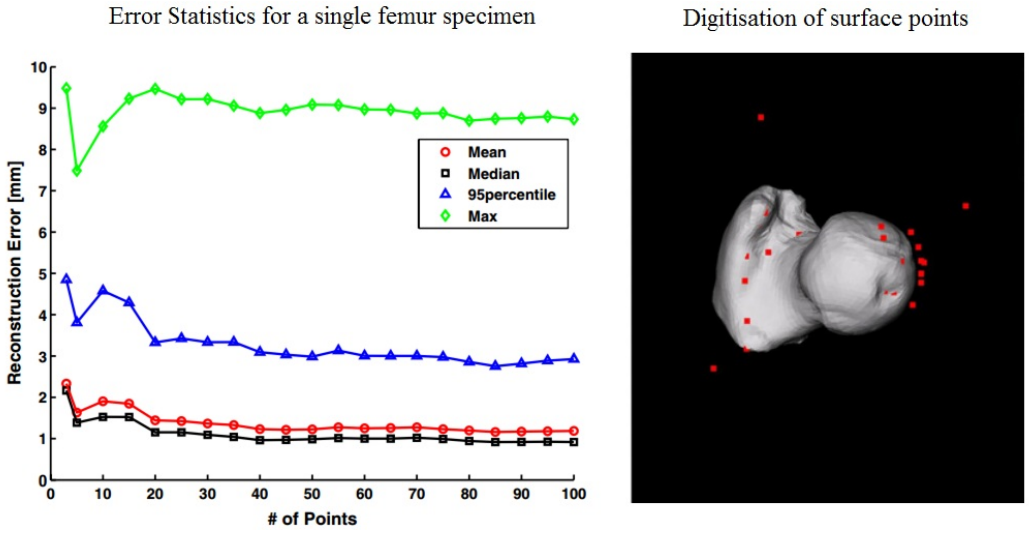

Figure 4.8: Shape estimation of the proximal femur based on a sparse input of digitised points. (a) Error statistics for a single femur specimen, (b) Surface points digitised using a pointer in a navigation environment (Image: Rajmani *et al.*, 2007).

Furthermore, a cadaver validation study was also carried out in which 9 different dry femur bones were used. A navigated pointer using an optical tracking system (accuracy of tracking system was within 1 mm) was utilised to digitise points off the dry bones (Figure 4.8(b)). Here, 30 proximal femurs were used in the construction of the SSM and the mean surface errors for the 9 dry cadaver bones was calculated using 3, 27 and 54 digitised surface points. The mean surface error here was found to be 2.17, 2.01 and 1.76 mm when using 3, 27 and 54 digitised surface points, respectively. The results for predicting the cadaver bones were found to be in the same error range as the leave-one-out experiments therefore it was concluded that a reasonably accurate prediction of the 3D shape can be obtained even with only very sparse information. Lastly, the use of ultrasound for the digitisation of surface points was also explored by Rajmani *et al.* (2007) on two cast femur bones. The accuracy of the automatic segmentation scheme for the extraction of the digitised points had a mean accuracy of 0.42 mm. The mean surface errors obtained (averaged over 5 attempts) using this technique were found to be 4.59 and 3.95 mm with each of the two bones, respectively. The results contained in this work focused on the femur appear to be in agreement with that presented in Section 4.3.

4.5.4 AR concept application and simulated procedure

The results presented in Section 4.4 indicate that fluoroscopic guidance provided superior levels of accuracy in this case compared to that of AR guidance, with the mean accuracy under fluoroscopic guidance only being marginally su-

perior (lower mean error and less variance). This result may be biased towards the surgeon being more comfortable with what he/she is used to (in this case fluoroscopic guidance is the "norm") whereas with using AR guidance which is somewhat unfamiliar, only a few trial runs were undertaken prior to recording any results officially. Statistically speaking, the values obtained from conducting an F and T-test on the results from an accuracy standpoint indicate a statistically significant difference in the variance but no significant difference between the means of the two populations.

From a time-to-completion perspective, undertaking the simulated procedure under AR guidance is markedly faster. The results from conducting an F and T-test on the time-to-completion recordings indicate a statistically significant difference in the means but not in variance between the two sets of data. It can thus be concluded that AR guidance appears to show potential for shortening procedural times. Even though superior accuracy was observed here under fluoroscopic guidance, AR guidance does not expose both the patient and surgeon to any harmful ionising radiation and this is a significant upside to making use of this form of navigational assistance.

Final user feedback in the form of a post-procedure debriefing was obtained from the Advanced Orthopaedic Training Centre (AOTC) representative (Dr Rudolph Venter) who conducted all of the simulated procedures and provided the following comments with regards to the tests carried out as well as his thoughts on utilising AR to assist with navigation during orthopaedic surgery:

> *In my opinion, a major drawback of modern commercially available surgical guidance systems is the fact that they are very cumbersome and very expensive. A surgical guidance system is just that: A system to help a surgeon complete a procedure he/she was trained to do unguided, better. As soon as a guidance system becomes difficult to operate, it negates the relative benefit.*
>
> *AR assistance in the form illustrated in this thesis potentially brings all the benefits of existing systems in a package that interferes very little with the normal workflow in theatre. My learning curve on the prototype system was very good and delivered a comparable level of accuracy with no radiation exposure. When interpreting the results from this study, one has to bear in mind that a video see-through display was used, so essentially I was handicapped in a sense that I did not have normal stereoscopic vision (i.e. no depth perception).*

A study conducted by Wang *et al.* (2015) (given as one of the case studies in Section 2.6) investigated the use of AR to assist with the insertion of percuta-

neous sacroiliac screws. The mean deviation between the planned trajectories and the inserted screws was 2.7±1.2 mm at the bony entry point, 3.7±1.1 mm at the screw tip, and the mean angular deviation between the two trajectories was 2.9°±1.1°. The mean deviation at the nerve root tunnels region on the sagittal plane was 3.6±1.0 mm. A similar study conducted by Citak *et al.* (2006) navigated percutaneous pelvic sacroiliac screw fixation using fluoroscopy. In this study minimal perforation of the cortex was seen in 15 % of screw placements and more severe perforation in 5 % of the cases. A separate study by Jacob *et al.* (1997) aimed at assessing the midterm results of closed reduction and percutaneous CT-guided sacroiliac screw fixation. Here 93% of screws were placed correctly with no impingement of the screws on neurovascular structures.

The second study given in Section 2.6 by Abe *et al.* (2013) investigates the use of AR to assist with navigation during percutaneous vertebroplasty (PVP). Computed tomography analysis of the 40 spine phantom trials showed that the error of the insertion angle (EIA) in the axial plane significantly improved when virtual protractor with augmented reality (VIPAR) was used compared with when it was not used (i.e. only under fluoroscopic guidance) (0.96°±0.61° vs 4.34°±2.36°, respectively). The same held true for EIA in the sagittal plane (0.61°±0.70° vs 2.55°±1.93°, respectively). The clinical results (involving 5 patients) showed that the EIA in all 10 needle insertions was 2.09°±1.3° and 1.98°±1.8° in the axial and sagittal plane, respectively. Another study by van der Kraats *et al.* (2006) looked at the accuracy of using 3D rotational X-ray navigation for needle guidance in percutaneous vertebroplasty. Here the average distance between the navigated needle tip and the real position of the needle tip was 2.5±1.5 mm.

Lastly, a study conducted by Chen *et al.* (2015) investigated the use of a optical see-through head-mounted display to assist with surgical navigation. Here the precision verification process of the navigation system included all aspects leading up to, and during a typical AR-guided surgical procedure (CT scanning, 3D reconstruction/segmentation, calibration of surgical instruments, registration, calibration of head-mounted display, real-time motion tracking, etc.). A probe was used to measure 100 target points and 30 axial holes in different regions after which the distance and angular errors were calculated. The accuracy verification experiment demonstrated that the mean distance and angular errors were 0.809±0.05 mm and 1.038°±0.05°, which was deemed sufficient to meet the clinical requirements.

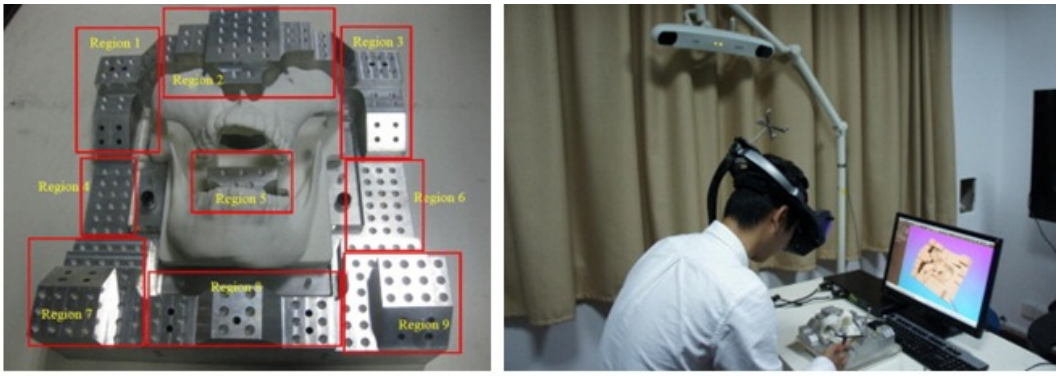

Figure 4.9: Precision verification process of the AR navigation system. (a) The accuracy verification block, (b) The accuracy verification of AR-based surgical navigation system. (Image: Rajmani *et al.*, 2007)

In conclusion, literature does appear to support the idea that AR navigation has the potential to provide comparable accuracy compared to other surgical navigation systems currently in use (such has fluoroscopy and CT-based navigation systems). The accuracy levels achieved in this study appear to agree with those found in literature and although the results here indicate that fluoroscopic guidance was superior in this case, the advantages such as the shortening in procedure duration and the reduction or even elimination of ionising radiation exposure are evident.

Chapter 5

Conclusion and recommendations

This chapter includes the conclusions drawn from the experimental process with special attention given to addressing how the project aims and objectives set out in Chapter 1 have been met. Recommendations for future studies relating to the tools and techniques used here as well as studies relating to augmented reality-assisted orthopaedic surgery (ARAOS) in general are also given.

5.1 Conclusion

Revisiting the aim of this study which was to investigate the clinical efficacy and feasibility of an application of ARAOS technology that focuses on supporting and enhancing current best practises in orthopaedic surgery, each of the objectives which were set out towards successfully achieving this are now evaluated. The first objective involved identifying a clinical problem which would be suitable for an initial proof-of-concept ARAOS study. Through consultation with a representative from the Advanced Orthopaedic Training Centre (AOTC) at Tygerberg Hospital, wrist replacement surgery was chosen as the clinical problem on which focus would be placed for this particular study.

The second objective set out for this study was to conceptualise a procedural workflow based around the chosen clinical problem aimed at providing streamlined and affordable navigational assistance. A workflow aimed at providing maximum benefit for these types of procedures was conceptualised which would involve making use of the two surgically removed bones to predict the remaining geometry by incorporating a statistical shape model (SSM) into a shape estimation process. Points were digitised off the two removed bones (using two different methods) in order to obtain the partial input which was then used for estimating the full shape of the geometry in question. This estimate of the patient's geometry can then be exported and ideally used in conjunction with an augmented reality (AR) device providing a continuous heads up view of

patient specific anatomical information. Thus potentially providing for scan-free navigation and a reduction in radiation exposure for both the patient and surgeon. Although there is room for improvement with regards to the digitisation process, this conceptual workflow does appear to be a viable option. It is the author's opinion that what has been mentioned here contributes to the successful completion of the second objective initially set out.

In terms of the third and fourth objectives which included the development of a smartphone-based ARAOS application and validating its effectiveness *in vitro*, a simple but effective experiment was designed which would allow for a comparison to be made between using conventional navigational methods and that of using AR guidance to assist with surgical navigation. The results from this experiment indicate marginally inferior accuracy compared to the more conventional fluoroscopic guidance, a reduction in procedural time, and a relatively short learning curve (intuitiveness) being observed when using AR guidance. Furthermore, with AR navigational assistance, both the patient and the surgeon are not exposed to harmful ionising radiation sources. With regards to the experimental process followed as well as the results obtained, it is believed that the questions posed in Section 3.5 have been answered and that the the third and fourth objectives set out for the successful completion of this study have been met.

In conclusion, it is the author's opinion that ARAOS technology appears to show clinical efficacy and feasibility for use in the operating room with potential to support and enhance current best practises in orthopaedic surgery while remaining affordable and potentially more intuitive than other forms of navigational assistance.

5.2 Recommendations

A number of issues were encountered during the course of completing this study which provide for recommendations to be made with respect to any future studies in a similar field or on any of the subtopics covered here. Firstly, with regards to the statistical shape modelling aspect of this study, there appeared to be a lack of useful morphological data on all four of the bones utilised here which made the selection of reliable anatomical landmarks problematic. The selection of reliable anatomical landmarks is beneficial when constructing a SSM (i.e. during rough alignment prior to establishing correspondence) as well as when digitising landmarks on the two surgically removed bones (scaphoid and lunate) for shape estimation purposes. In this study, anatomical landmarks were simply chosen based on the authors intuition. Thus it may be recommended that in future, a detailed morphological study be conducted prior to undertaking statistical shape analysis to identify the most reliable

anatomical features which could be used for landmark selection.

One significant limitation with the SSM constructed in this study is that it lacks information pertaining to the relative pose and scale within a single set of four bones (third metacarpal, capitate, lunate and scaphoid - from one individual). In this case, all four bones were each scaled to unity and centered at the origin and therefore the output from the statistical shape modelling process is again a set of four bones, each centered at the origin and scaled to unity. It was proposed in Section 4.5.1 that one possible solution to this problem would be to make use of a second, simpler SSM aimed at modelling the relative pose and scale within the group of four bones. The output from the first shape model would thus be used as an initial estimate into the second shape model. Furthermore, literature relating to the use of articulated statistical shape models (ASSM) was given in Section 4.5.1 and such methods may also provide for a suitable solution in this case. Alternatively, another potential solution would be to try model the four bones as a single entity (scaling the set of bones to unity and centering this set at the origin), however, it is unsure as to whether this would cause issues when attempting to establish correspondence and may also result in physically impossible joint configurations (overlapping of adjacent shapes - this was discussed in Section 4.5.1). These possible solutions are areas to explore should any future work in this area be carried out.

From an AR perspective, AR was used on two occasions during the course of this study. The first being that in the point digitisation process and the second was to provide navigational assistance during the simulated AR-guided procedure. In terms of the AR-based point digitising application, the errors observed were relatively significant considering the scale of the objects being digitised. It is thought that the source of error may be because of ill-scaled registration of the augmented reality content onto the real world geometry. It may be necessary to incorporate calibration procedures into the AR application itself, or during its construction within the AR environment used (in this case being the Unity Game Engine). With regards to the AR concept application used for navigational assistance during the simulated procedure, unfortunately the head-mounted display (HMD) used in this study was of the video see-through (VST) type. These displays do not offer the user a sense of depth when making use of his/her hands and thus relies solely on the navigational guidance provided through the AR application to carry out the procedure. An optical see-through (OST) HMD was purchased late into this study, but due to time constraints it was not able to be integrated into the Unity Game Engine, hence the VST display was opted for. The VST display still proved to be an intuitive form of navigational assistance and therefore the use of an OST display in any future studies in this area would only further improve the intuitiveness and usability of this technology and is strongly recommended.

Lastly, although not done here, the smooth integration of all the constituents comprising the procedural workflow outlined in Section 3.1.3 is a potential area of focus for future work. This would also involve the design of a simulated procedure more realistic and in line with the actual procedural workflow described in Section 3.1.2.

References

3d-microscribe.com. (2017). MicroScribe G2X Digitizer. [online] Available at: http://www.3d-microscribe.com/G2%20Page.htm [Accessed 11 Aug. 2017].

3D FilaPrint. Available at: https://3dfilaprint.com/category/photon-3d-scannerupdates/ [Accessed 11 Aug. 2017].

Abe, Y., Sato, S., Kato, K., Hyakumachi, T., Yanagibashi, Y., Ito, M. and Abumi, K. (2013). A novel 3D guidance system using augmented reality for percutaneous vertebroplasty. Journal of Neurosurgery: Spine, 19(4), pp.492-501.

Anon, (2017). [image] Available at: https://forum.maxwellrender.com/viewtopic.php?t=10486 [Accessed 13 Jul. 2017].

Besl and McKay, 1992 Besl, P.J., and Neil D. McKay. (1992). "A Method For Registration Of 3-D Shapes". *IEEE Transactions on Pattern Analysis and Machine Intelligence 14.2* p.239-256. Web.

Bic.mni.mcgill.ca. (2017). Conventional Stereotaxy. [online] Available at: http://www.bic.mni.mcgill.ca/users/patrice/msthesis/node10.html [Accessed 10 Aug. 2017].

Bindernagel, M., Kainmueller, D., Ramm, H., Lamecker, H., Zachow, S. (2012). Analysis of inter-individual anatomical shape variations of joint structures. Zuse Institute Berlin, Berlin, Germany.

Birkfellner, W., Hummel, J., Wilson, E. (2008). In: Peters, T., Cleary, K. (eds), Image-Guided Interventions. Springer.

Blackwell, M., Morgan, F. and DiGioia, A. (1998). Augmented Reality and Its Future in Orthopaedics. *Clinical Orthopaedics and Related Research*, 354, pp.111-122.

Blakeney WG, Khan RJ, Wall SJ. Computer-assisted techniques versus conventional guides for component alignment in total knee arthroplasty: a ran-

domized controlled trial. J Bone Joint Surg Am. 2011;93:1377-1384. doi: 10.2106/JBJS.I.01321.

Blanc, R., Syrkina, E. and Szekely, G. (2009). "Estimating the confidence of statistical model based shape prediction". In: *Information Processing in Medical Imaging*, pp. 602-613. Springer.

Blanz, V., Mehl, A., Vetter, T. and Seidel, H.-P. (2004). "A statistical method for robust 3d surface reconstruction from sparse data." In: *3D Data Processing, Visualization and Transmission, 2004. 3DPVT 2004. Proceedings. 2nd International Symposium on*, pp. 293-300. IEEE.

CAD House. (2017). bqLabs CiClop 3D Scanner by-Scan Anything. [online] Available at: http://www.cad-house.co.za/ciclop.html [Accessed 11 Aug. 2017].

Chen, X., Xu, L., Wang, Y., Wang, H., Wang, F., Zeng, X., Wang, Q. and Egger, J. (2015). Development of a surgical navigation system based on augmented reality using an optical see-through head-mounted display. Journal of Biomedical Informatics, 55, pp.124-131.

Citak, M., Hufner, T., Geerling, J., Kfuri, M., GÃ¤nsslen, A., Look, V., Kendoff, D. and Krettek, C. (2006). Navigated percutaneous pelvic sacroiliac screw fixation: Experimental comparison of accuracy between fluoroscopy and Iso-C 3D navigation. Computer Aided Surgery, 11(4), pp.209-213.

ClaroNav. (2017). History of Surgical Navigation Technology - ClaroNav. [online] Available at: http://www.claronav.com/history-of-surgical-navigation-technology/ [Accessed 14 Jul. 2017].

Cootes, T.F., Taylor, C.J., Cooper, D.H., Graham, J. (2001). "Training Models Of Shape From Sets Of Examples." Manchester: Department of Medical Biophysics, University of Manchester.

Crisco, Joseph J., Coburn, J.C., Moore, D.C., Upal, M.A. (2005). "Carpal Bone Size And Scaling In Men Versus In Women". *The Journal of Hand Surgery* 30.1 35-42. Web.

Davies, Rhodri H., Cootes, Tim F., Twining, Carole J., Taylor, Chris J. (2002). "An Information Theoretic Approach To Statistical Shape Modelling." University of Manchester.

Dessenne V, Lavallee S, Julliard R, *et al.*, (1995) Computer assisted knee anterior cruciate ligament reconstruction: first clinical tests. J Image Guid Surg; 1: 59-64.

Diffen.com (2017). MRI vs X-ray - Difference and Comparison | Diffen. [online] Available at: http//www.diffen.com/difference/MRI-vs-X-ray [Accessed 10 Aug. 2017].

Enchev, Y. (2009). Neuronavigation: geneology, reality, and prospects. Neurosurgical FOCUS, 27(3), p.E11.

Ericsson, Anders, and Johan Karlsson. (n.d.) "Benchmarking Of Algorithms For Automatic Correspondence Localisation." Lund, Sweden: Centre for Mathematical Sciences, Lund University.

Eu.xyzprinting.com. (2017). da Vinci 1.0 AiO | 3D Printer | Product - XYZprinting |3D printer models | domestic 3D printers | 3D printers. [online] Available at: http://eu.xyzprinting.com/eu-en/Product/da-Vinci-1.0-AiO [Accessed 11 Aug. 2017].

Explained Visually. (2017). Principal Component Analysis explained visually. [online] Available at: http://setosa.io/ev/principal-component-analysis/ [Accessed 28 Aug. 2017].

Fleute M, Lavallee S, Julliard R (1999) Incorporating a statistically based shape model into a system for computer assisted anterior cruciate ligament surgery. Med Imag Anal; 3: 209-222.

Ganz, J. (2014). Gamma knife neurosurgery. [Place of publication not identified]: Springer.

Gelfand, N., Ikemoto, L., Rusinkiewics, S., Levoy, M. (n.d.). "Geometrically Stable Sampling For The ICP Algorithm". Print.

GoMeasure3D. (2017). MicroScribe Affordable Portable CMM | GoMeasure3D. [online] Available at: http://gomeasure3d.com/microscribe/ [Accessed 11 Aug. 2017].

Grimm, F., Naros, G., Gutenberg, A., Keric, N., Giese, A. and Gharabaghi, A. (2015). Blurring the boundaries between frame-based and frameless stereotaxy: feasibility study for brain biopsies performed with the use of a head-mounted robot. Journal of Neurosurgery, 123(3), pp.737-742.

Heiland M, Schulze D, Adam G, et al. (2003) 3D-imaging of the facial skeleton with an isocentric mobile C-arm system (Siremobil Iso-C3D). Dentomaxillofac Radiol; 321: 21-25.

Hofstetter R, Slomczykowski M, Bourquin Y, et al. Fluoroscopy based surgical navigation: concept and clinical applications. In: Lemke HU, Vannier MW, Inamura K (1997) Computer Assisted Radiology and Surgery. Amsterdam:

Elsevier Science; 956-960.

Hofstetter R, Slomczykowski M, Sati M, *et al.*, (1999) Fluoroscopy as an imaging means for computer-assisted surgical navigation. Comput Aided Surg; 4: 65-76.

Hopkinsmedicine.org. (2017). Burr holes | Johns Hopkins Medicine Health Library. [online] Available at: http://www.hopkinsmedicine.org/healthlibrary/test-procedures/neurological/burr-holes-135,318/ [Accessed 10 Aug. 2017]

Imaginis.com. (2017). Brief History of CT | CT Scan | Imaginis - The Women's Health & Wellness Resource Network. [online] Available at: http://www.imaginis.com/ct-scan/brief-history-of-ct [Accessed 10 Aug. 2017].

Impactscan.org. (2017). impactscan.org | a brief history of CT. [online] Available at: https://www.impactscan.org/CThistory.htm [Accessed 10 Aug. 2017]

Jacob, A., Messmer, P., Stock, K., Suhm, N., Baumann, B., Regazzoni, P. and Steinbrich, W. (1997). Posterior pelvic ring fractures: Closed reduction and percutaneous CT-guided sacroiliac screw fixation. Cardiovascular and Interventional Radiology, 20(4), pp.285-294.

Jaramaz B, DiGioia AM, Blackwell M, *et al.*, (1998) Computer assisted measurement of cup placement in total hip replacement. Clin Orthop; 354: 70-81.

Kainmueller, D., Lamecker, H., Zachow, S., Hege, H.C. (2009). An articulated statistical shape model for accurate hip joint segmentation.

Kersten-Oertel, M., Jannin, P. and Collins, D. (2013). The state of the art of visualization in mixed reality image guided surgery. *Computerized Medical Imaging and Graphics*, 37(2), pp.98-112.

Kijima, Y. and Viegas, S. (2009). Wrist Anatomy and Biomechanics. The Journal of Hand Surgery, 34(8), pp.1555-1563.

Kilgore, E. and Elster, A. (1995). Walter Dandy and the history of ventriculography. Radiology, 194(3), pp.657-660.

Knowcas.com. (2017). About CAS. [online] Available at: http://knowcas.com/about [Accessed 10 Aug. 2017]

Koivukangas, T., Katisko, J.P.A., Koivukangas, J.P. (2013). Technical accuracy of optical and the electromagnetic tracking systems. SpringerPlus. https://doi.org/10.1186/2193-1801-2-90

Laine T, Lund T, Ylikoski M, et al. (2000) Accuracy of pedicle screw insertion

with and without computer assistance: a randomised controlled clinical study in 100 consecutive patients. Eur Spine J; 9: 235-240.

Lamata, P., Ali, W., Cano, A., *et al.*, (2010). Augmented Reality for Minimally Invasive Surgery: Overview and Some Recent Advances, Augmented Reality, Soha Maad (Ed.), InTech, DOI: 10.5772/7128. Available from: https://www.intechopen.com/books/augmented-reality/augmented-reality-for-minimally-invasive-surgery-overview-and-some-recent-advances

Langlotz, F. (2004). Potential pitfalls of computer aided orthopedic surgery. Injury, 35(1), pp.17-23.

Lavallee S (1996) Registration for computer-integrated surgery: methodology, start of the art. In: Taylor RH, Lavallee S, Burdea GC, et al. (1996) Computer Integrated Surgery. Cambridge. The MIT Press: 77-97.

Lehnen K, Giesinger K, Warschkow R, Porter M, Koch E, Kuster MS. Clinical outcome using a ligament referencing technique in CAS versus conventional technique. Knee Surg Sports Traumatol Arthrosc. 2010;19(6):887-892. doi: 10.1007/s00167-010-1264-4.

Livyatan, H., Yaniv, Z., Joskowicz, L., 2003. Gradient-based 2-D/3-D rigid registration of fluoroscopic X-ray to CT. IEEE Transactions on Medical Imaging 22 (11), 1395-1406.

Maintz JBA, Viergever MA (1998) A survey of medical image registration. Med Image Anal; 2: 1-36.

MakerBot. (2017). MakerBot Digitizer Desktop 3D Scanner | Order Today!. [online] Available at: https://www.makerbot.com/media-center/2013/08/22/makerbot-digitizer-desktop-3d-scanner-order-today [Accessed 11 Aug. 2017].

Matterandform.net. (2017). Matter and Form. [online] Available at: https://matterandform.net/scanner [Accessed 11 Aug. 2017].

McInerney, J. and Roberts, DW. (200). Frameless stereotaxy of the brain. Mt Sinai J Med. 2000 Sep; 67(4):300-10.

Medicalexpo.com. (2017). MedicalExpo - The online Medical Exhibition: medical device, medical imaging, hospital furniture, laboratory equipement .... [online] Available at: http://www.medicalexpo.com/ [Accessed 14 Jul. 2017].

MedicalExpo (2017). [image] Available at: http://www.medicalexpo.com/prod/brainlab/product-75290-545859.html [Accessed 13 Jul. 2017].

Metavision.com. (2016). Augmented Reality - Home | Meta Company. [online]

Available at: https://www.metavision.com/ [Accessed 13 Jun. 2016].

Mezger, U., Jendrewski, C. and Bartels, M. (2013). Navigation in surgery. *Langenbecks Arch Surg*, 398(4), pp.501-514.

Microsoft HoloLens. (2017). Microsoft HoloLens. [online] Available at: https://www.microsoft.com/en-us/hololens [Accessed 13 Jul. 2017].

Myronenko, Andriy and Xubo Song. "Point Set Registration: Coherent Point Drift". *IEEE Transactions on Pattern Analysis and Machine Intelligence* 32.12 (2010): 2262-2275. Web.

Nde-ed.org. (2017). History. [online] Available at: https://www.nde-ed.org/EducationResources/CommunityCollege/Radiography/Introduction/history.htm. Accessed 10 Aug 2017.

Neurosurgery.org. (2017). Cyber Museum of Neurosurgery. [online] Available at: http://www.neurosurgery.org/cybermuseum/stereotactichall/stereoarticle.-html [Accessed 10 Aug. 2017].

Nikou, C., Digioia, A., Blackwell, M., Jaramaz, B. and Kanade, T. (2000). Augmented reality imaging technology for orthopaedic surgery. *Operative Techniques in Orthopaedics*, 10(1), pp.82-86.

Nolte LP, Visarius H, Arm E, et al. (1995) Computer-aided fixation of spinal implants. J Imag Guid Surg; 1: 88-93.

Okamoto, T., Onda, S., Yanaga, K., Suzuki, N. and Hattori, A. (2014). Clinical application of navigation surgery using augmented reality in the abdominal field. Surgery today, vol. 45, no. 4, pp. 397-406.

Orringer, D., Golby, A., and Jolesz, F. (2012). Neuronavigation in the surgical management of brain tumors: current and future trends. Expert Review of Medical Devices, 9(5), pp.491-500.

Peng, L., Guangyao, L., Xiao, M., Xie, L. (2016). "Robust CPD Algorithm For Non-Rigid Point Set Registration Based On Structure Information." *PLOS ONE 11.2* Web.

Peters, T.M., Evans, A.C., Olivier, A. (1994). Frameless Stereotaxy. In: Shorvon S.D., Fish, D.R., Andermann, F., Bydder, G.M., Stefan, H. (eds) Magnetic Resonance Scanning and Epilepsy. NATO ASI Series (Series A: Life Sciences), vol 264. Springer, Boston, MA.

Phillips, B. (2017). Wrist Joint Anatomy: Overview, Gross Anatomy, Natural Variants. [online] Emedicine.medscape.com. Available at: https://emedicine.m-

edscape.com/article/1899456-overview-a1 [Accessed 4 Aug. 2017].

Polhemus.com. (2017). Polhemus Digitizing Systems. [online] Available at: http://polhemus.com/scanning-digitizing/digitizing-products/ [Accessed 11 Aug. 2017].

Prod.cubify.com. (2017). Sense 3D Scanner | Features | 3D Systems. [online] Available at: https://prod.cubify.com/sense [Accessed 11 Aug. 2017].

Radiologyinfo.org. (2017). Brain Imaging, functional (fMRI). [online] Available at: https://www.radiologyinfo.org/en/info.cfm?pg=fmribrain [Accessed 10 Aug. 2017]

Radiopaedia.org. (2017). Articles | Radiopaedia.org. [online] Available at: http://radiopaedia.org/articles [Accessed 10 Aug. 2017].

Rajamani, K., Styner, M., Talib, H., Zheng, G., Nolte, L. and Ballester, M. (2007). Statistical deformable bone models for robust 3D surface extrapolation from sparse data. Medical Image Analysis, 11(2), pp.99-109.

Rivkin G, Liebergall M. Challenges of technology integration and computer-assisted surgery. J Bone Joint Surg Am. 2009;91(Suppl 1):13-16. doi: 10.2106/JBJS.H.01410.

Rock C, Linsenmaier U, Brandl R, et al. (2001) Vorstel-lung eines neuen mobilen C-Bogen-/CT-Kombinationsgerat(ISO-C3D)-Erste Ergebnisse der 3D-Schnittbildgebung. Unfallchirurg; 104: 827-833.

Sarkalkan, Nazli, Harrie Weinans, and Amir A. Zadpoor. "Statistical Shape And Appearance Models Of Bones". Bone 60 (2014): 129-140. Web.

"Scann3d : Smartmobilevision". Scann3d.smartmobilevision.com. N.p., 2017. Web. 16 Apr. 2017.

Schep NW, Broeders IA, van der Werken C (2003) Computer-assisted orthopaedic and trauma surgery. State of the art and future perspectives. Injury; 34: 299-306.

SearchHealthIT. (2017). What is PACS (picture archiving and communication system)? - Definition from WhatIs.com. [online] Available at: http://searchhealthit.techtarget.com/definition/picture-archiving-and-communication-system-PACS [Accessed 10 Aug. 2017].

Sebastian, T., Tek, H., Crisco, J. and Kimia, B. (2003). Segmentation of carpal bones from CT images using skeletally coupled deformable models. Medical Image Analysis, 7(1), pp.21-45.

Seebright - Developer Kit & Environment for Mixed Reality. (2017). Home. [online] Available at: https://seebright.com/ [Accessed 13 Jul. 2017].

Seeger, W. and Zentner, J. (2002). Neuronavigation and neuroanatomy. Wien: Springer.

Shuhaiber, J. (2004). Augmented Reality in Surgery. *Arch Surg*, 139(2), p.170.

Stegmann, Mikkel B., and David Delgado Gomez. (2002). *A Brief Introduction To Statistical Shape Analysis.* Lyngby, Denmark: Technical University of Denmark.

Store.google.com. (2017). Google Cardboard - Official VR Headset - Google Store. [online] Available at: https://store.google.com/us/product/google-cardboard?hl=en-US [Accessed 13 Jul. 2017].

Su, Zihua. (2011). "Statistical Shape Modelling: Automatic Shape Model Building". Ph.D. University College London.

Swemac | With passion for innovation. [online] Swemac.com. Available at: http://www.swemac.com/ [Accessed 14 Jul. 2017].

Textbook of Stereotactic and Functional Neurosurgery. (2009). Berlin: Springer, pp.619-629.

TopTenReviews. Cubify Sense 3D Review - Pros, Cons and Verdict. Available at: http://www.toptenreviews.com/computers/scanners/best-3d-scanners/cubify-review/ [Accessed 11 Aug. 2017].

UTCT - University of Texas. (2017). Resolution and Size Limitations | UTCT - University of Texas. [online] Available at: http://www.ctlab.geo.utexas.edu/about-ct/resolution-and-size-limitations/ [Accessed 11 Aug. 2017].

Wang, H., Wang, F., Leong, A., Xu, L., Chen, X. and Wang, Q. (2015). Precision insertion of percutaneous sacroiliac screws using a novel augmented reality-based navigation system: a pilot study. *International Orthopaedics (SICOT).*

Woodworth GF, McGirt MJ, Samdani A, *et al.* Frameless image-guided stereotactic brain biopsy procedure: diagnostic yield, surgical morbidity, and comparison with the frame-based technique. J Neurosurg. 2006;104:233-237.

Wyawahare, M.V., Patil, P.M., Abhyankar, H.K. (2009). Image Registration Techniques: An Overview. International Journal of Signal Processing, Image Processing and Pattern Recognition. Vol.2, No.3, September 2009.